



Queensland University of Technology
Brisbane Australia

This may be the author's version of a work that was submitted/accepted for publication in the following source:

Zhou, Ying, Zhan, Haifei, Zhang, Weihong, Zhu, Jihong, Bai, Jinshuai, Wang, Qingxia, & Gu, YuanTong
(2020)

A new data-driven topology optimization framework for structural optimization.

Computers & Structures, 239, Article number: 106310.

This file was downloaded from: <https://eprints.qut.edu.au/207974/>

© 2020 Elsevier Ltd.

This work is covered by copyright. Unless the document is being made available under a Creative Commons Licence, you must assume that re-use is limited to personal use and that permission from the copyright owner must be obtained for all other uses. If the document is available under a Creative Commons License (or other specified license) then refer to the Licence for details of permitted re-use. It is a condition of access that users recognise and abide by the legal requirements associated with these rights. If you believe that this work infringes copyright please provide details by email to qut.copyright@qut.edu.au

License: Creative Commons: Attribution-Noncommercial 4.0

Notice: *Please note that this document may not be the Version of Record (i.e. published version) of the work. Author manuscript versions (as Submitted for peer review or as Accepted for publication after peer review) can be identified by an absence of publisher branding and/or typeset appearance. If there is any doubt, please refer to the published source.*

<https://doi.org/10.1016/j.compstruc.2020.106310>

A new data-driven topology optimization framework for structural optimization

Ying Zhou^{a,b}, Haifei Zhan^a, Weihong Zhang^{b,*}, Jihong Zhu^b, Jinshuai Bai^a, Qingxia Wang^c, Yuantong Gu^{a,*}

^aSchool of Mechanical, Medical and Process Engineering, Queensland University of Technology, Brisbane, QLD 4001, Australia

^bState IJR Center of Aerospace Design and Additive Manufacturing, Northwestern Polytechnical University, Xi'an, Shaanxi 710072, China

^cBusiness School, The University of Queensland, Brisbane, QLD 4072, Australia

*Corresponding author: yuantong.gu@qut.edu.au (Y. Gu); zhangwh@nwpu.edu.cn (W. Zhang)

Abstract

The application of structural topology optimization with complex engineering materials is largely hindered due to the complexity in phenomenological or physical constitutive modeling from experimental or computational material data sets. In this paper, we propose a new data-driven topology optimization (DDTO) framework to break through the limitation with the direct usage of discrete material data sets in lieu of constitutive models to describe the material behaviors. This new DDTO framework employs the recently developed data-driven computational mechanics for structural analysis which integrates prescribed material data sets into the computational formulations. Sensitivity analysis is formulated by applying the adjoint method where the tangent modulus of prescribed uniaxial stress-strain data is evaluated by means of moving least square approximation. The validity of the proposed framework is well demonstrated by the truss topology optimization examples. The proposed DDTO framework will provide a great flexibility in structural design for real applications.

Keywords: Topology optimization, Constitutive model, Material data set, Data-driven computational mechanics, Moving least square.

1. Introduction

Topology optimization is gaining exponentially growing applications in a wide

range of industries such as civil, automotive, aerospace and others [1–4]. It has been recognized as an advanced design method for lightweight and high-performance structures [5,6]. The majority of topology optimization approaches are dedicated to linear elastic structures whose boundary value problem can be formulated as linear system of equations and solved efficiently. However, many engineering structures are beyond the scope of linear systems which normally undergo geometric nonlinearity, material nonlinearity (e.g. hyperelasticity, elastoplasticity and heterogeneity etc.) or both. As such, great efforts have been devoted to topology optimization with different sources of nonlinearities [7–11].

Material nonlinearity is one of the main concerns in nonlinear topology optimization. Traditionally, material nonlinearity is tackled with the phenomenological or physical constitutive models which are calibrated from experimental measurements or theoretical calculations through fitting or regression techniques [12,13]. For instances, various hyperelastic models have been developed for rubberlike materials and applied in topology optimization of soft-bodied structures [14–17]. Different elastoplastic models in terms of elastic modulus, plastic hardening parameter and yield stress have also been utilized in structural optimization with elastoplastic metals/alloys and reinforced composites [18–22]. Nevertheless, the derivation of empirical constitutive models for complex engineering materials, such as composites, ceramics, polymers and geological materials, remains a challenging problem worldwide due to the complexities of material behaviors related to intrinsic and extrinsic factors such as phase change, strain rate and multiphysics coupling etc.

Therefore, it is of great interest to ask whether the empirical constitutive models can be avoided in structural topology optimization. The thriving big data and machine learning techniques as being popularly applied for computational mechanics and material designs in the past few years [23–26], provide new clues for this question. The deep neural network was explored as a powerful method for the approximation of field variables to solve the boundary value problems in both strong and weak forms [23,24]. The data-driven computations with an offline training/learning process based on computational homogenization followed by an online constitutive prediction were developed for heterogeneous materials using deep convolution neural networks [27–30]. The developed data-driven neural networks are applied to reduce computational costs and improve the efficiency of microstructure-based or multiscale topology optimization designs [30–33].

Very recently, a new paradigm of data-driven computational mechanics is developed [34–37] to integrate the experimental or computational material data into the computational formulations without the requirement of constitutive modeling. In their works, the stress and strain states of a structure are calculated by searching the material data set and conservation laws of compatibility and equilibrium to minimize their distance in energy-based sense. Ibanez etc. [38] mapped the high-dimensional phase spaces of stress and strain into low-dimensional constitutive manifolds and realized real-time computations using manifold learning. Herein, inspired by aforementioned works, we propose a new data-driven topology optimization (DDTO) framework. Unlike the previous topology optimization approaches based on data-driven neural networks, this new DDTO framework uses directly discrete material data set collected from experimental measurements or theoretical calculations for the description of material behaviors, thereby bypasses the phenomenological or physical constitutive modeling process. This work is expected to provide a great flexibility in structural design when no prior knowledge of analytic constitutive model is available.

The remainder of this paper is organized as follows. Section 2 introduces concisely the traditional topology optimization framework in which analytic constitutive models are used. Section 3 introduces the new DDTO framework in which discrete material data sets are directly used. Numerical examples are illustrated in section 4. Conclusions and future perspectives are outlined in section 5.

2. Traditional topology optimization framework

Topology optimization methods have been developed for structural design of both discrete and continuum structures. To have a straightforward idea of topology optimization with material nonlinearity, this paper adopts truss topology optimization as benchmark problems due to its simple constitutive relationship between uniaxial strain ε and uniaxial stress σ . For comparison purpose, the traditional topology optimization framework shown in Fig. 1 is concisely discussed.

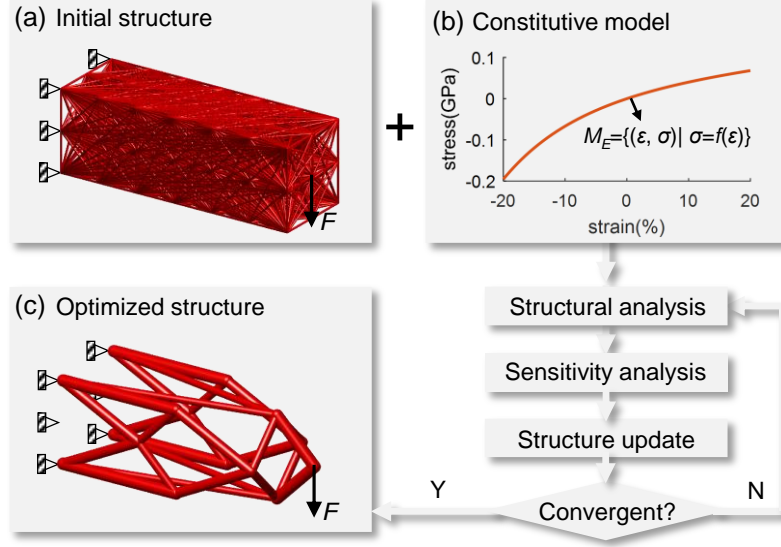


Fig. 1. Traditional topology optimization framework: (a) geometry, loading and boundary conditions of initial structure; (b) constitutive model $M_E = \{(\varepsilon, \sigma) \mid \sigma = f(\varepsilon)\}$ which describes analytically the relationship between strain and stress; (c) optimized structure.

2.1. Basic formulations of topology optimization problem

Ground structure method is the most popular method for truss topology optimization. This method defines the initial ground structure by connecting a set of pre-distributed nodes with potential bar elements and achieves topology variation by varying the cross-sectional areas of these bar elements with the possibility of zero-valued area. Fig. 1(a) shows an initial structure defined by a full-level ground structure [39]. Notice that the ground structure can be a subset of the full-level structure.

Without loss of generality, consider the topology optimization problem which minimizes the structural end-compliance while satisfies prescribed material volume constraint. It is mathematically stated as

$$\begin{aligned}
 \min_{\mathbf{A}} \quad & J(\mathbf{A}, \mathbf{u}) = \mathbf{F}_{\text{ext}}^T \mathbf{u} \\
 \text{subject to} \quad & \mathbf{R}(\mathbf{A}, \mathbf{u}) = \mathbf{F}_{\text{ext}} - \mathbf{F}_{\text{int}} = \mathbf{0} \\
 & V(\mathbf{A}) = \sum_{e=1}^m A_e L_e \leq V_{\text{max}} \\
 & A_e \geq 0, \quad e = 1, 2, \dots, m
 \end{aligned} \tag{1}$$

where m denotes the number of potential bar elements in ground structure. L_e denotes the axial length of the e -th bar. $\mathbf{A} = (A_1, A_2, \dots, A_m)$ refers to the vector of design variables

related to cross-sectional areas. Notice that A_e is continuously variable in the non-negative real number space R^+ , whereas in numerical implementation an extremely small value α is usually attributed as the lower bound to prevent the singularity of stiffness matrix [40]. \mathbf{u} denotes the nodal displacement vector under external force \mathbf{F}_{ext} . $\mathbf{R}(\mathbf{A}, \mathbf{u})$ stands for the residual between external force \mathbf{F}_{ext} and internal force \mathbf{F}_{int} and $\mathbf{R}(\mathbf{A}, \mathbf{u})=\mathbf{0}$ indicates the equilibrium of concerned structure. J and V are structural end-compliance and volume, respectively. V_{max} is the upper bound of volume constraint.

2.2. Structural analysis with Newton-Raphson method

- **Boundary value Problems**

Boundary value problems in science and engineering typically combine two types of laws: (i) conservation laws derived from universal principles such as conservation of momentum or energy; and (ii) material law between stress and strain for the description of material behavior. To make it clear, both laws for truss structures are formulated as follows.

(i) Conservation laws of equilibrium and compatibility

Assume that the concerned structure is limited within elastic deformation. The potential energy of an elastic truss structure is expressed as

$$\Pi(\mathbf{u}) = \Pi^{\text{int}}(\mathbf{u}) - \Pi^{\text{ext}}(\mathbf{u}) = \sum_{e=1}^m \int_{A_e} \int_{L_e} W(\varepsilon_e) dAdL - \mathbf{F}_{\text{ext}}^T \mathbf{u} \quad (2)$$

where Π^{int} and Π^{ext} denote the strain energy and total work of external load, respectively. $W(\varepsilon_e)$ denotes strain energy density relevant to strain ε_e which satisfies the *compatibility equation* $\varepsilon_e = \mathbf{B}_e \mathbf{u}$ ($e=1,2,\dots,m$). Notice that in elasticity the stress σ_e can be obtained by differentiating W with respect to ε_e .

According to the principle of minimum potential energy and variational method, the *governing equation of equilibrium* is stated as

$$\sum_{e=1}^m \int_{A_e} \int_{L_e} \sigma_e^T(\mathbf{u}) \varepsilon_e(\mathbf{v}) dAdL = \mathbf{F}_{\text{ext}}^T \mathbf{v} \quad \forall \mathbf{v} \in S \quad (3)$$

where S denote 1-order Sobolev space. \mathbf{v} is kinetically admissible test function. Notice that Dirichlet boundary condition $\mathbf{u}=\mathbf{u}_0$ on Γ_D is needed to avoid rigid-body motion.

(ii) Constitutive models

Conventionally, the phenomenological or physical constitutive models $M_E = \{(\varepsilon, \sigma) |$

$\sigma=f(\varepsilon)\}$ which describe analytically the relationship between strain and stress ensure the closedness of boundary value problem. To date, a variety of constitutive models have been developed for hyperelastic, elastoplastic or heterogeneous materials. To give an example, several hyperelastic models under the assumption of uniaxial deformation [16] are given in Table 1.

Table 1. Typical hyperelastic models with the assumption of uniaxial deformation [16].

Type	Strain energy density W	Constitutive model	Material parameters
Ogden	$W = \sum_{i=1}^I \frac{\gamma_i}{\beta_i} (\lambda^{\beta_i} - 1)$	$\sigma = \sum_{i=1}^I \gamma_i \lambda^{\beta_i-1}$	$\lambda=\varepsilon+1$ where λ denotes the linearized stretch;
St Venant	$W = \frac{E}{8} (\lambda^2 - 1)^2$	$\sigma = \frac{E}{2} (\lambda^3 - \lambda)$	Young's modulus $E=A+2\mu$
Neo-Hookean	$W = \frac{E}{4} (\lambda^2 - 1 - 2 \ln \lambda)$	$\sigma = \frac{E}{2} (\lambda - \lambda^{-1})$	where A and μ denotes Lamé constants;
Henky	$W = \frac{E}{2} (\ln \lambda)^2$	$\sigma = \frac{E}{\lambda} \ln \lambda$	$I \geq 1$, γ_i and β_i are material parameters

- **Newton-Raphson method**

As is well known, the Newton-Raphson method is effective in solving the boundary value problem with general nonlinearity. It starts from an initial guess of displacement \mathbf{u}^k ($k=0$). Suppose $\mathbf{R}(\mathbf{u}^k) \neq 0$, the guess of solution is updated by

$$\begin{cases} \mathbf{K}^{\tan} \Delta \mathbf{u}^k = \mathbf{F}_{\text{ext}} - \mathbf{F}_{\text{int}}(\mathbf{u}^k) \\ \mathbf{u}^{k+1} = \mathbf{u}^k + \Delta \mathbf{u}^k \end{cases} \quad (4)$$

where $\Delta \mathbf{u}^k$ denotes incremental displacement. \mathbf{K}^{\tan} and \mathbf{F}_{int} refer to the tangent stiffness matrix and internal force related to current state of \mathbf{u}^k , which are mathematically expressed as

$$\begin{cases} \mathbf{K}^{\tan}(\mathbf{u}^k) = \sum_{e=1}^m \int_{A_e} \int_{L_e} \mathbf{B}_e^T D_e^{\tan} \mathbf{B}_e dA dL \\ \mathbf{F}_{\text{int}}(\mathbf{u}^k) = \sum_{e=1}^m \int_{A_e} \int_{L_e} \mathbf{B}_e^T \sigma_e(\mathbf{u}^k) dA dL \end{cases} \quad (5)$$

in which the tangent modulus D_e^{\tan} can be analytically calculated from prescribed constitutive model $M_E = \{(\varepsilon, \sigma) | \sigma = f(\varepsilon)\}$. Note that constant stiffness matrix \mathbf{K} is usually used in replacement of \mathbf{K}^{\tan} to avoid the time-consuming reassembly and inverse calculation of large-scale \mathbf{K}^{\tan} in each iteration.

The iterative method terminates when $|\mathbf{R}(\mathbf{u}^K)| < \delta$ with δ referring to a prescribed small value, e.g. $\alpha = 10^{-6} \sim 10^{-8}$. In other words, the equilibrium between external and

internal forces reaches when $\mathbf{u}=\mathbf{u}^K$.

2.3. Sensitivity analysis for structural topology optimization

Sensitivity analysis is necessary to implement gradient-based optimization. The adjoint method [8] is generally applied in topology optimization with general nonlinearity. By introducing the adjoint vector $\boldsymbol{\beta}$ of equilibrium equation $\mathbf{R}(\mathbf{A}, \mathbf{u}^K)=\mathbf{0}$, the design objective in Eq. (1) can be modified as $J'(\mathbf{A}, \mathbf{u}^K)=\mathbf{F}_{\text{ext}}^T \mathbf{u}^K + \boldsymbol{\beta}^T \mathbf{R}$. In this work, \mathbf{F}_{ext} is assumed to be invariant with respect to the variation of design variables. The derivative of J' with respect to A_e reads

$$\frac{\partial J'}{\partial A_e} = \mathbf{F}_{\text{ext}}^T \frac{\partial \mathbf{u}^K}{\partial A_e} + \boldsymbol{\beta}^T \left(\frac{\partial \mathbf{R}}{\partial \mathbf{u}^K} \frac{\partial \mathbf{u}^K}{\partial A_e} + \frac{\partial \mathbf{R}}{\partial A_e} \right) = \left(\mathbf{F}_{\text{ext}}^T - \boldsymbol{\beta}^T \mathbf{K}^{\text{tan}}(\mathbf{u}^K) \right) \frac{\partial \mathbf{u}^K}{\partial A_e} - \boldsymbol{\beta}^T \frac{\partial \mathbf{F}_{\text{int}}}{\partial A_e} \quad (6)$$

By utilizing the arbitrariness of $\boldsymbol{\beta}$, the first term of the right-hand side in Eq. (6) can be eliminated by imposing $\mathbf{K}^{\text{tan}}(\mathbf{u}^K) \boldsymbol{\beta} = \mathbf{F}_{\text{ext}}$. The sensitivity of J is calculated as

$$\frac{\partial J}{\partial A_e} = -\boldsymbol{\beta}^T \frac{\partial \mathbf{F}_{\text{int}}}{\partial A_e} \quad (7)$$

where the term $\partial \mathbf{F}_{\text{int}} / \partial A_e$ is calculated by

$$\frac{\partial \mathbf{F}_{\text{int}}}{\partial A_e} = \partial \left(\sum_{e=1}^m \int_{A_e} \int_{L_e} \mathbf{B}_e^T \boldsymbol{\sigma}_e^K dA dL \right) / \partial A_e = L_e \mathbf{B}_e^T \boldsymbol{\sigma}_e^K \quad (8)$$

3. Data-driven topology optimization framework

We introduce the new data-driven topology optimization (DDTO) framework in this section. Fig. 2 shows the general framework of the DDTO which uses directly material data sets for the representation of material behaviors, rather than the empirical constitutive models.

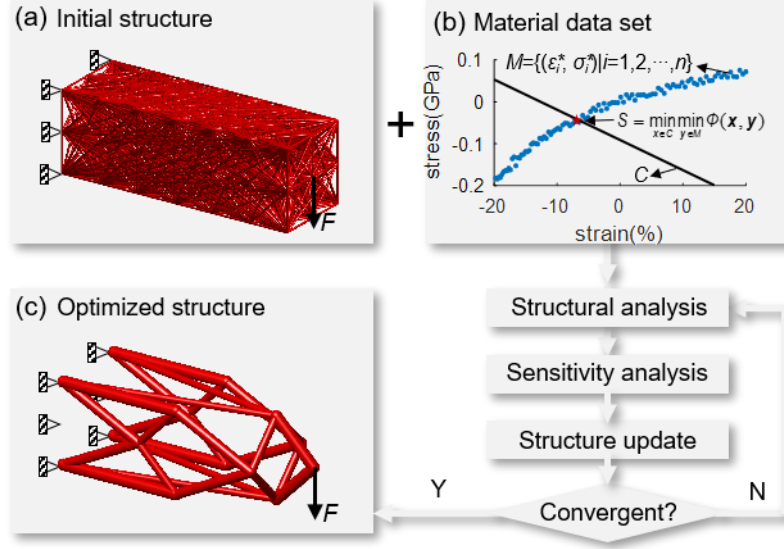


Fig. 2. Data-driven topology optimization (DDTO) framework: (a) geometry, loading and boundary conditions of initial structure; (b) $M = \{z_i^* = (\varepsilon_i^*, \sigma_i^*) | i=1, 2, \dots, n\}$ denotes the material data set, while C denotes the set of conservation laws of equilibrium and compatibility. In the data-driven computational mechanics, the solution of boundary value problem is to find the local states (ε, σ) which minimizes an energy-based distance between C and M ; (c) optimized structure.

3.1. Data-driven computational mechanics

The data-driven computational mechanics initially proposed by Kirchdoerfer and Ortiz [34–36] is recognized as a generalization of classical methods in which the material behavior is defined in terms of material data sets rather than empirical models. It possesses the advantage of high-fidelity description of material behavior.

As shown in Fig. 2(b), the data-driven computational mechanics is elaborately devised to find the local stress and strain states of bar members $\{z_e = (\varepsilon_e, \sigma_e) | e=1, 2, \dots, m\}$ which minimizes the distance between conservation set C and material data set M [34]

$$\min_{(\varepsilon_e^*, \sigma_e^*) \in M} \min_{(\varepsilon_e, \sigma_e) \in C} \Phi = \sum_{e=1}^m \int_{A_e} \int_{L_e} \Psi(\varepsilon_e - \varepsilon_e^*) + \Psi'(\sigma_e - \sigma_e^*) dA dL \quad (9)$$

where $\Psi(\varepsilon)$ and $\Psi'(\sigma)$ denote the reference strain energy density and complementary energy density, respectively.

$$\Psi(\varepsilon_e) = \frac{1}{2} \varepsilon_e^T D_e \varepsilon_e, \quad \Psi'(\sigma_e) = \frac{1}{2} \sigma_e^T D_e^{-1} \sigma_e \quad (10)$$

in which D_e denotes an arbitrary constant modulus. In Eq. (9), the distance metric in a

local phase space of each bar member is defined as

$$d(z_e, z_e^*) = \left(\frac{1}{2} (\varepsilon_e - \varepsilon_e^*)^T D_e (\varepsilon_e - \varepsilon_e^*) + \frac{1}{2} (\sigma_e - \sigma_e^*)^T D_e^{-1} (\sigma_e - \sigma_e^*) \right)^{1/2} \quad (11)$$

The data-driven problem in Eq. (9) is solved iteratively by decomposing into inner and outer subproblems. It begins with an initial guess $\{z_e^{*0} = (\varepsilon_e^{*0}, \sigma_e^{*0}) \mid e=1,2,\dots,m\}$ from material data set M for each bar element.

- Inner subproblem

The inner subproblem aims to find $\{z_e^k = (\varepsilon_e^k, \sigma_e^k) \mid e=1,2,\dots,m\}$ closest to $\{z_e^{*k} = (\varepsilon_e^{*k}, \sigma_e^{*k}) \mid e=1,2,\dots,m\}$ while satisfying the conservation laws of compatibility and equilibrium equations.

$$\begin{aligned} \min_{(\varepsilon_e^k, \sigma_e^k)} : \quad & \Phi = \sum_{e=1}^m \int_{A_e} \int_{L_e} \Psi(\varepsilon_e^k - \varepsilon_e^{*k}) + \Psi'(\sigma_e^k - \sigma_e^{*k}) dAdL \\ \text{subject to: } & \varepsilon_e^k = \mathbf{B}_e \mathbf{u}^k \quad e = 1, 2, \dots, m \\ & \sum_{e=1}^m \int_{A_e} \int_{L_e} \mathbf{B}_e^T \sigma_e^k dAdL = \mathbf{F}_{\text{ext}} \end{aligned} \quad (12)$$

By applying the Lagrange multiplier and variational methods, above constrained optimization problem can be solved as [34]

$$\begin{aligned} \varepsilon_e^k &= \mathbf{B}_e \mathbf{u}^k \\ \sigma_e^k &= D_e \mathbf{B}_e \boldsymbol{\lambda}^k + \sigma_e^{*k} \end{aligned} \quad e=1,2,\dots,m \quad (13)$$

where $\boldsymbol{\lambda}^k$ denotes the Lagrange multiplier vector of the equilibrium equation. \mathbf{u}^k and $\boldsymbol{\lambda}^k$ are calculated by solving the following linear equation systems

$$\begin{aligned} \mathbf{K} \mathbf{u}^k &= \mathbf{F}_\varepsilon^k \\ \mathbf{K} \boldsymbol{\lambda}^k &= \mathbf{F}_{\text{ext}} - \mathbf{F}_\sigma^k \end{aligned} \quad (14)$$

with

$$\begin{aligned} \mathbf{K} &= \sum_{e=1}^m \int_{A_e} \int_{L_e} \mathbf{B}_e^T D_e \mathbf{B}_e dAdL \\ \mathbf{F}_\varepsilon^k &= \sum_{e=1}^m \int_{A_e} \int_{L_e} \mathbf{B}_e^T D_e \varepsilon_e^{*k} dAdL \\ \mathbf{F}_\sigma^k &= \sum_{e=1}^m \int_{A_e} \int_{L_e} \mathbf{B}_e^T \sigma_e^{*k} dAdL \end{aligned} \quad (15)$$

- Outer subproblem

Consequently, the outer subproblem is solved to find $\{z_e^{*k+1} = (\varepsilon_e^{*k+1}, \sigma_e^{*k+1}) \mid e=1,2,\dots,m\}$ which is closest to the $\{z_e^k = (\varepsilon_e^k, \sigma_e^k) \mid e=1,2,\dots,m\}$ calculated in Eq. (13).

$$\min_{(\varepsilon_e^{*k+1}, \sigma_e^{*k+1}) \in M} \Phi = \sum_{e=1}^m \int_{A_e} \int_{L_e} \Psi(\varepsilon_e^k - \varepsilon_e^{*k+1}) + \Psi'(\sigma_e^k - \sigma_e^{*k+1}) dAdL \quad (16)$$

Due to the non-negativity of Ψ and Ψ' as defined in Eq. (10), the outer subproblem Eq. (16) can be further decomposed into m nearest neighbor search problems

$$\min_{(\varepsilon_e^{*k+1}, \sigma_e^{*k+1}) \in M} \varphi_e = \Psi(\varepsilon_e^k - \varepsilon_e^{*k+1}) + \Psi'(\sigma_e^k - \sigma_e^{*k+1}) \quad e = 1, 2, \dots, m \quad (17)$$

Note that **noises may exist** in the data sets due to the intrinsic stochasticity of material behavior, experimental and environmental variability etc. Nevertheless, the nearest neighbor search problems in Eq. (17) overemphasize the influence of individual nearest point, rather than a clustering of multiple nearest points. To overcome the problem that noisy data might be closer to $z_e^k = (\varepsilon_e^k, \sigma_e^k)$, the **cluster analysis technique considering multiple nearest neighbors is utilized**. To this end, each point $\{z_i^* = (\varepsilon_i^*, \sigma_i^*) | i=1, 2, \dots, n\}$ in the material data set is assigned a probability according to its distance to z_e^k [36]

$$p_i(z_e^k, \beta^k) = \frac{e^{-\beta^k d^2(z_e^k, z_i^*)}}{\sum_{i=1}^n e^{-\beta^k d^2(z_e^k, z_i^*)}} \quad (18)$$

In Eq. (18), the parameter β^k controls the number of data points in concerned cluster. $\beta^k=0$ indicates that all points are considered in the cluster with identical probabilities. In contrast, the nearest neighbor search in Eq. (17) is recovered when $\beta^k \rightarrow +\infty$. For finite β^k , Eq. (18) complies with the Boltzmann distribution that the probability decreases along with the increase of $d(z_e^k, z_i^*)$.

The choice of β^k follows a simulated annealing scheme [36]. Initially, β^0 is set to be small to cast a broad net that all points in the data set influence the solution. Subsequently, the annealing temperature $1/\beta^k$ decreases, i.e. β^k increases, to narrow the cluster that only finite points influence the solution.

$$\frac{1}{\beta^0} = \sum_{e=1}^m \frac{1}{n} \left(\sum_{i=1}^n d^2(\bar{z}_e^0, z_i^*) \right), \quad \bar{z}_e^0 = \frac{1}{n} \sum_{i=1}^n z_i^* \quad (19)$$

$$\beta^{k+1} = (1 - \mu) \tilde{\beta}^{k+1} + \mu \beta^k \quad (20)$$

where μ is a prescribed annealing rate. In this paper, the annealing rate is set $\mu=0.1$ for all numerical examples. $\tilde{\beta}^{k+1}$ is calculated as

$$\tilde{\beta}^{k+1} = \left(\sum_{e=1}^m \sum_{i=1}^n e^{-\beta^k d^2(z_e^k, z_i^*)} d^2(\bar{z}_e^k, z_i^*) \right) / \left(\sum_{e=1}^m \sum_{i=1}^n e^{-\beta^k d^2(z_e^k, z_i^*)} \right)^{-1} \quad (21)$$

The outer subproblem in Eq. (16) is finally solved as

$$\begin{aligned} \varepsilon_e^{*k+1} &= \bar{\varepsilon}_e^{k+1} = \sum_{i=1}^n p_i(z_e^k, \beta^k) \varepsilon_i^* \\ \sigma_e^{*k+1} &= \bar{\sigma}_e^{k+1} = \sum_{i=1}^n p_i(z_e^k, \beta^k) \sigma_i^* \end{aligned} \quad (22)$$

The iterative data-driven computation terminates at the K -th iteration if $(\varepsilon_e^{K+1}, \sigma_e^{K+1}) = (\varepsilon_e^K, \sigma_e^K)$ holds for all bar elements. The local states $\{(\varepsilon_e^K, \sigma_e^K) | e=1, 2, \dots, m\}$ constitute the solution of the boundary value problem.

Note 1: It is evident that the local states $\{(\varepsilon_e^K, \sigma_e^K) | e=1, 2, \dots, m\}$ satisfy the conservation law of equilibrium. According to Eq. (13), the internal force $\mathbf{F}_{\text{int}}(\mathbf{u}^k)$ can be expressed as

$$\begin{aligned} \mathbf{F}_{\text{int}} &= \sum_{e=1}^m \int_{A_e} \int_{L_e} \mathbf{B}_e^T \sigma_e^k dA dL \\ &= \left(\sum_{e=1}^m \int_{A_e} \int_{L_e} \mathbf{B}_e^T D_e \mathbf{B}_e dA dL \right) \boldsymbol{\lambda}^k + \sum_{e=1}^m \int_{A_e} \int_{L_e} \mathbf{B}_e^T \sigma_e^{*k} dA dL \\ &= \mathbf{K} \boldsymbol{\lambda}^k + \mathbf{F}_{\sigma}^k = \mathbf{F}_{\text{ext}} \end{aligned} \quad (23)$$

Clearly, the residual $\mathbf{R}(\mathbf{u}^k) = \mathbf{F}_{\text{ext}} - \mathbf{F}_{\text{int}}(\mathbf{u}^k)$ equals zero for $\{(\varepsilon_e^K, \sigma_e^K) | e=1, 2, \dots, m\}$.

3.2. Sensitivity analysis with discrete material data sets

With the data-driven computational mechanics, the structural end-compliance can be formulated as follows and shown to be identical with the classic form in Eq. (1).

$$\begin{aligned} J(\mathbf{A}, \mathbf{u}^K) &= \sum_{e=1}^m \int_{A_e} \int_{L_e} (\sigma_e^K)^T \varepsilon_e^K dA dL \\ &= \sum_{e=1}^m \int_{A_e} \int_{L_e} (D \mathbf{B}_e \boldsymbol{\lambda}^K + \sigma_e^{*K})^T (\mathbf{B}_e \mathbf{u}^K) dA dL \\ &= (\mathbf{K} \boldsymbol{\lambda}^K + \mathbf{F}_{\sigma}^K)^T \mathbf{u}^K \\ &= \mathbf{F}_{\text{ext}}^T \mathbf{u}^K \end{aligned} \quad (24)$$

Recalling $\mathbf{R}(\mathbf{A}, \mathbf{u}^K) = \mathbf{0}$ as in Eq. (23), the adjoint method can also be utilized for the sensitivity derivation. Similar to section 2.3, the sensitivity of design objective $J(\mathbf{A}, \mathbf{u}^K)$

with respect to design variable A_e reads

$$\frac{\partial J}{\partial A_e} = -\boldsymbol{\beta}^T \frac{\partial \mathbf{F}_{\text{int}}}{\partial A_e} \quad (25)$$

where $\partial \mathbf{F}_{\text{int}} / \partial A_e$ can be calculated as Eq. (8). The adjoint variable $\boldsymbol{\beta}$ can be obtained by solving

$$\frac{\partial \mathbf{F}_{\text{int}}}{\partial \mathbf{u}^K} \boldsymbol{\beta} = \mathbf{F}_{\text{ext}} \quad (26)$$

with

$$\frac{\partial \mathbf{F}_{\text{int}}}{\partial \mathbf{u}^K} = \sum_{e=1}^m \int_{A_e} \int_{L_e} \mathbf{B}_e^T \frac{\partial \sigma_e^K}{\partial \varepsilon_e^K} \mathbf{B}_e dA dL \quad (27)$$

In Eq. (27), $\partial \sigma_e^K / \partial \varepsilon_e^K$ is needed to calculate locally based on data points which may irregularly distribute. In this paper, for the ease of calculation of $\partial \sigma_e^K / \partial \varepsilon_e^K$, the stress state σ_e^K is locally fitted by means of moving least square (MLS) approximation [41]. The MLS approximation has been proven accurate and robust with a global continuity in fitting complex surfaces based on arbitrarily distributed points [41,42]. In MLS, σ_e^K is expressed as the linear combination of the product of MLS shape functions and stress values at the data points within a support domain of ε_e^K

$$\sigma_e^K(\varepsilon_e^K) = \sum_{i_e=1}^{N_e} \phi_{i_e}(\varepsilon_e^K) \sigma_{i_e}^* = \boldsymbol{\phi}^T(\varepsilon_e^K) \boldsymbol{\sigma}^* \quad (28)$$

where $\boldsymbol{\sigma}^* = [\sigma_1^*, \sigma_2^*, \dots, \sigma_{N_e}^*]^T$ is the stress array at N_e data points within the support domain. $\boldsymbol{\phi}(\varepsilon_e^K) = [\phi_1(\varepsilon_e^K), \phi_2(\varepsilon_e^K), \dots, \phi_{N_e}(\varepsilon_e^K)]^T$ is array of MLS shape functions and expressed as [41]

$$\boldsymbol{\phi}(\varepsilon_e^K) = \mathbf{p}^T(\varepsilon_e^K) \mathbf{A}^{-1}(\varepsilon_e^K) \mathbf{B}(\varepsilon_e^K) \quad (29)$$

in which $\mathbf{p}(\varepsilon_e^K) = [p_1(\varepsilon_e^K), p_2(\varepsilon_e^K), \dots, p_l(\varepsilon_e^K)]^T$ denotes the basis function. In this work, a linear basis function $\mathbf{p}(\varepsilon_e^K) = [1, \varepsilon_e^K]^T$ is used. The matrices $\mathbf{A}(\varepsilon_e^K)$ and $\mathbf{B}(\varepsilon_e^K)$ are calculated as

$$\mathbf{A}(\varepsilon_e^K) = \sum_{i_e=1}^{N_e} w(\varepsilon_e^K - \varepsilon_{i_e}^*) \mathbf{p}(\varepsilon_{i_e}^*) \mathbf{p}^T(\varepsilon_{i_e}^*) \quad (30)$$

$$\mathbf{B}(\varepsilon_e^K) = \left[w(\varepsilon_e^K - \varepsilon_1^*) \mathbf{p}(\varepsilon_1^*), w(\varepsilon_e^K - \varepsilon_2^*) \mathbf{p}(\varepsilon_2^*), \dots, w(\varepsilon_e^K - \varepsilon_{N_e}^*) \mathbf{p}(\varepsilon_{N_e}^*) \right] \quad (31)$$

Without loss of generality, the Gauss weight function $w(\varepsilon_e^K - \varepsilon_{i_e}^*)$ is used in Eqs.

(30) and (31).

$$w(\varepsilon_e^K - \varepsilon_{i_e}^*) = \frac{e^{-\eta^2(\varepsilon_e^K - \varepsilon_{i_e}^*)^2/d_l^2} - e^{-\eta^2}}{1 - e^{-\eta^2}} \quad (32)$$

where d_l denotes the radius of support domain which usually needs to be determined numerically. η is a parameter of Gauss weight function where $\eta=3$ is often used in the literatures [41,42].

According to Eq. (28), the derivative $\partial\sigma_e^K/\partial\varepsilon_e^K$ reads

$$\frac{\partial\sigma_e^K(\varepsilon_e^K)}{\partial\varepsilon_e^K} = \sum_{i_e=1}^{N_e} \frac{\partial\phi_{i_e}(\varepsilon_e^K)}{\partial\varepsilon_e^K} \sigma_{i_e}^* \quad (33)$$

To proceed, the MLS shape function $\phi(\varepsilon_e^K)$ in Eq. (29) is firstly rewritten as

$$\phi(\varepsilon_e^K) = \gamma(\varepsilon_e^K) \mathbf{B}(\varepsilon_e^K) \quad (34)$$

where $\gamma(\varepsilon_e^K) = \mathbf{p}^T(\varepsilon_e^K) \mathbf{A}^{-1}(\varepsilon_e^K)$, i.e., $\mathbf{A}(\varepsilon_e^K) \gamma(\varepsilon_e^K) = \mathbf{p}(\varepsilon_e^K)$.

The derivative of MLS shape functions $\phi(\varepsilon_e^K)$ then follows

$$\frac{\partial\phi(\varepsilon_e^K)}{\partial\varepsilon_e^K} = \frac{\partial\gamma(\varepsilon_e^K)}{\partial\varepsilon_e^K} \mathbf{B}(\varepsilon_e^K) + \gamma(\varepsilon_e^K) \frac{\partial\mathbf{B}(\varepsilon_e^K)}{\partial\varepsilon_e^K} \quad (35)$$

where

$$\begin{cases} \frac{\partial\gamma(\varepsilon_e^K)}{\partial\varepsilon_e^K} = \mathbf{A}^{-1}(\varepsilon_e^K) \left(\frac{\partial\mathbf{p}}{\partial\varepsilon_e^K} - \frac{\partial\mathbf{A}}{\partial\varepsilon_e^K} \gamma(\varepsilon_e^K) \right) \\ \frac{\partial\mathbf{A}(\varepsilon_e^K)}{\partial\varepsilon_e^K} = \sum_{i_e=1}^{N_e} \frac{\partial w(\varepsilon_e^K - \varepsilon_{i_e}^*)}{\partial\varepsilon_e^K} \mathbf{p}(\varepsilon_{i_e}^*) \mathbf{p}^T(\varepsilon_{i_e}^*) \\ \frac{\partial\mathbf{B}(\varepsilon_e^K)}{\partial\varepsilon_e^K} = \left[\frac{\partial w(\varepsilon_e^K - \varepsilon_1^*)}{\partial\varepsilon_e^K} \mathbf{p}(\varepsilon_1^*), \frac{\partial w(\varepsilon_e^K - \varepsilon_2^*)}{\partial\varepsilon_e^K} \mathbf{p}(\varepsilon_2^*), \dots, \frac{\partial w(\varepsilon_e^K - \varepsilon_{N_e}^*)}{\partial\varepsilon_e^K} \mathbf{p}(\varepsilon_{N_e}^*) \right] \end{cases} \quad (36)$$

Note 2: The computational accuracy of $\partial\sigma_e^K/\partial\varepsilon_e^K$ in Eq. (33) is dependent upon the number of data points N_e in the support domain. A fundamental criterion requires that N_e should be large enough to avoid the singularity of weighted moment matrix $\mathbf{A}(\varepsilon)$. The best choice of N_e is difficult to get theoretically. Numerical investigations are needed in order to obtain high precision computation of $\partial\sigma_e^K/\partial\varepsilon_e^K$. Note that MLS is robust and a wide range of support domain can be used in MLS [41,42].

Note 3: In view of the arbitrariness of D_e in Eqs. (9)-(17), the derivatives $\partial\sigma_e^K/\partial\varepsilon_e^K$ in Eq. (33) can be used as an approximation of tangent modulus D_e^{tan} in replacement of D_e

to accelerate the convergence rate of the data-driven method.

Note 4: The detailed flowchart of the proposed DDTO framework for truss structures is shown in Fig. 3.

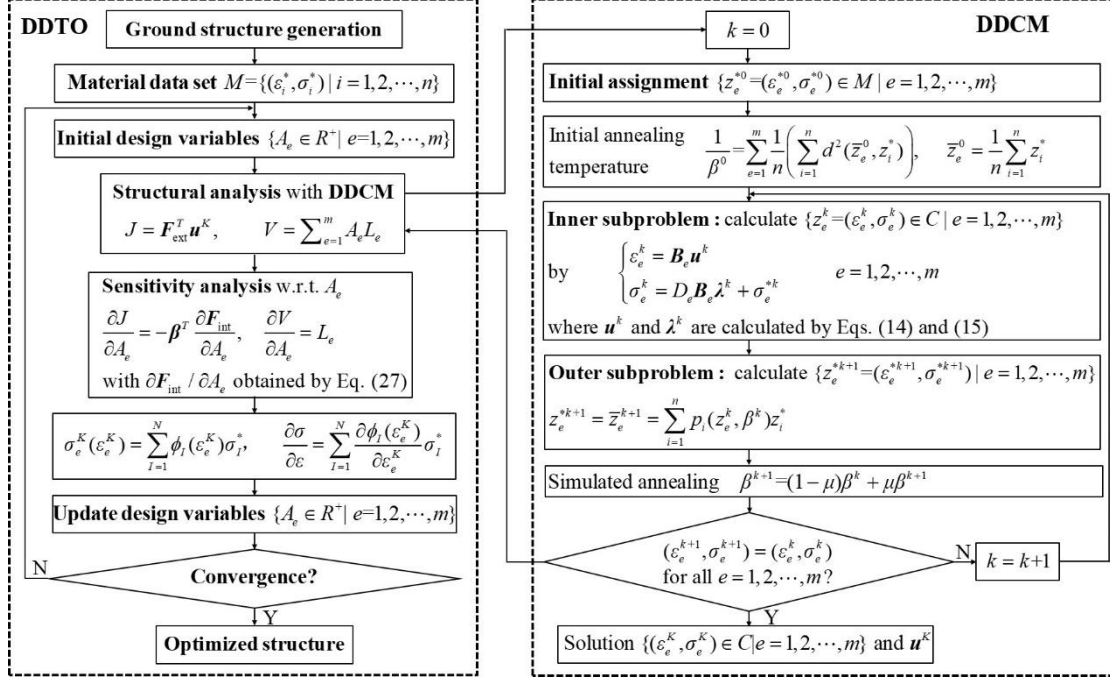


Fig. 3. The detailed flowchart of DDTO framework for truss structures. The dot box on left-hand side is the loops for structural optimization, while that on right-hand side is the **iterative data-driven computational mechanics (DDCM) for structural analysis**.

3.3. Numerical verification of data-driven computational mechanics and sensitivity analysis

As shown in Fig. 4(a), a simple tensile bar problem is adopted to instantiate the data-driven computational mechanics and sensitivity calculation formulated in Section 3.2. Relevant parameters are $A=5$, $L=10$ and $F=1$. The analytic solution is $\sigma=F/A=0.2$. For the sake of comparison, we consider the material data set illustrated in Fig. 4(b). The sampling of data points follows the Standard ASTM E8/E8M [43] for mechanical testing with the rate of straining control method. The rate of straining is set 1×10^{-3} . The data set is generated from the base Ogden model [44] and Gauss random noises with a proportion of 1% relative to the base stresses are added. As shown in Fig. 4(c), the tangent modulus D^{tan} evaluated by MLS agrees well with that by analytical differentiating the Ogden model. In MLS, the radius of support domain is $d_f=0.05$.

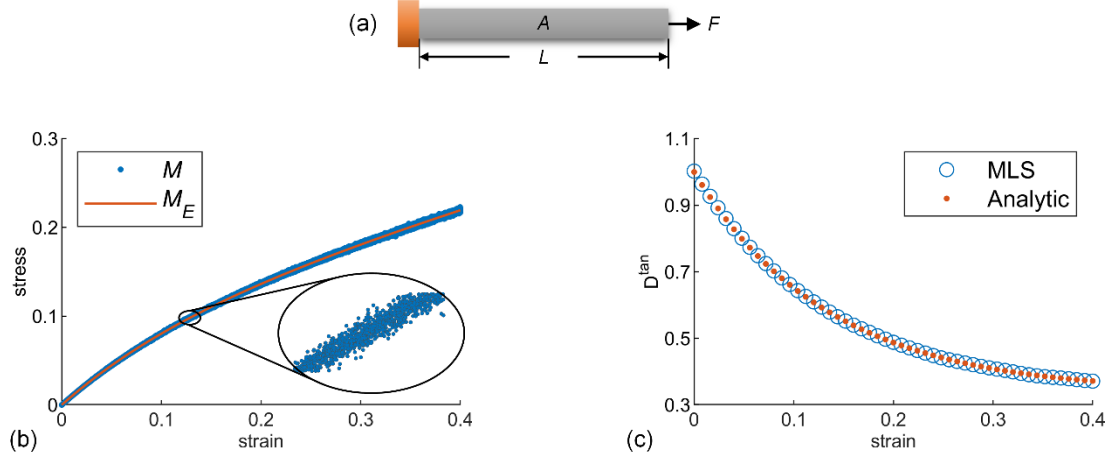


Fig. 4. A tensile bar problem for numerical verification of data-driven computational mechanics and sensitivity calculation: (a) geometry, loading and boundary conditions; (b) noisy data set M generated from Ogden model M_E ($I=2$, $\gamma_1=-\gamma_2=E/(\beta_1-\beta_2)$, $E=1$, $\beta_1=2.71$, $\beta_2=-4.73$), include Gauss random noises with a proportion of 1% relative to the base stresses; (c) tangent modulus D^{tan} calculated by analytically differentiating Ogden model as well as by MLS in Eq. (33).

Suppose the number of material data $n=10^4$. The iterative processes of both Newton-Raphson and data-driven methods with different values of constant modulus $D_e=1, 2, 4$ are depicted in Fig. 5. It is observed that D_e effects the convergence rate of both methods. Besides, as shown in Fig. 6, using tangent modulus D^{tan} instead of constant modulus D_e generally accelerates convergence. Nevertheless, as discussed in section 2.2, numerical burdens of the reassembly and inverse calculation of \mathbf{K}^{tan} in each iteration become heavy when D^{tan} is used, especially for large-scale problems.

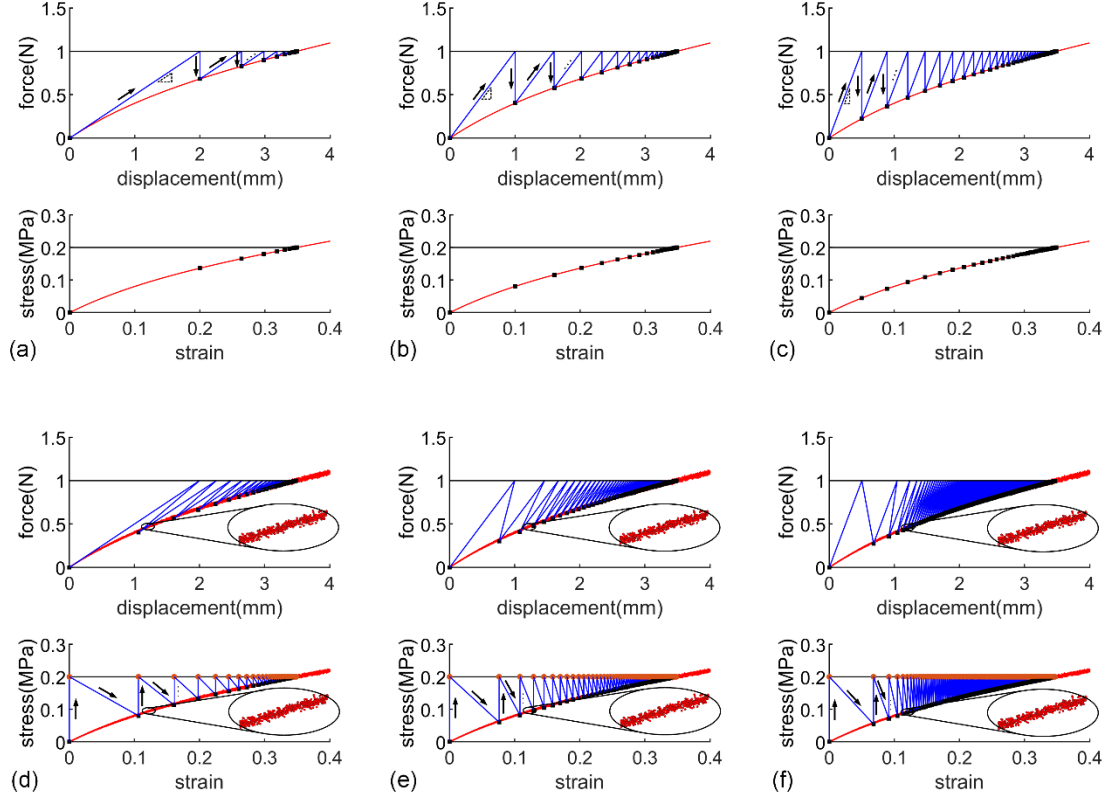


Fig. 5. The iterative processes of different methods with constant modulus D_e : (a) Newton-Raphson method ($D_e=1$); (b) Newton-Raphson method ($D_e=2$); (c) Newton-Raphson method ($D_e=4$); (d) data-driven method ($D_e=1$); (e) data-driven method ($D_e=2$); (f) data-driven method ($D_e=4$).

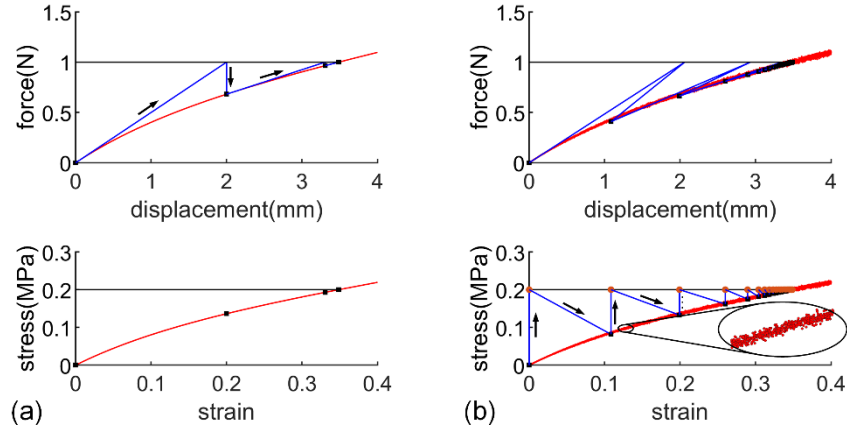


Fig. 6. The iterative processes of different methods with tangent modulus D^{\tan} : (a) Newton-Raphson method with D^{\tan} calculated based on analytic constitutive models; (b) data-driven method with D^{\tan} calculated by MLS in Eq. (33).

It is noticeable that the Newton-Raphson method diverges when constant modulus

$D_e=0.2$, as shown in Fig. 7(a). This is because D_e deviates too far from the tangent modulus D^{tan} in the first several iterations. Nevertheless, the data-driven method still converges due to a pullback operation to the prescribed strain range, as shown in Fig. 7(b). The relative errors of ε , σ , J and $\partial J/\partial A$ compared with analytic solutions are given in Table 2. High computational accuracies are obtained for both methods when $n=10^4$.

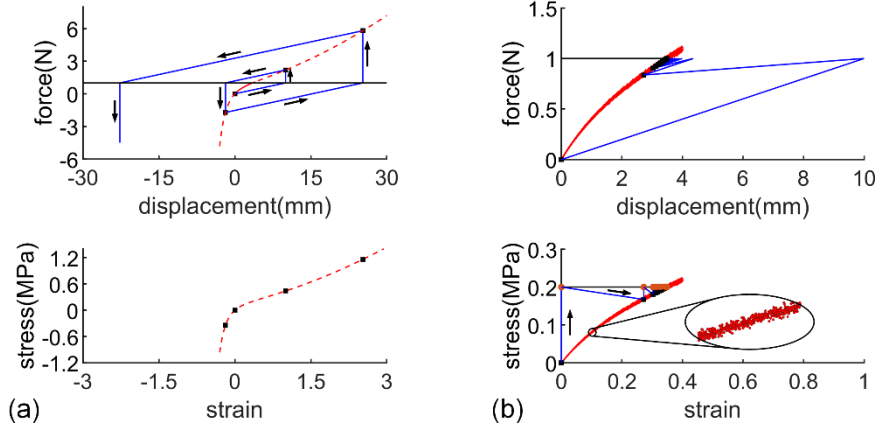


Fig. 7. The iterative processes of different methods with constant modulus $D_e=0.2$: (a) Newton-Raphson method; (b) data-driven method.

Table 2. Relative errors of ε , σ , J and $\partial J/\partial A$ as well as number of iterations for different method.

Method	D_e	e_ε (%)	e_σ (%)	e_J (%)	$e_{\partial J/\partial A}$ (%)	$n_{\text{iteration}}$
Newton-Raphson	0.2	-	-	-	-	-
	1	8.2231×10^{-7}	5.5507×10^{-7}	8.2231×10^{-7}	8.2434×10^{-7}	37
	2	1.0311×10^{-6}	6.9603×10^{-7}	1.0311×10^{-6}	1.0337×10^{-6}	84
	4	1.2642×10^{-6}	8.5333×10^{-7}	1.2642×10^{-6}	1.2673×10^{-6}	176
	D^{tan}	3.1830×10^{-14}	1.3878×10^{-14}	2.5464×10^{-14}	2.1486×10^{-14}	6
Data-driven	0.2	5.8770×10^{-2}	1.3878×10^{-14}	5.8770×10^{-2}	0.8484	28
	1	2.8231×10^{-2}	0	2.8231×10^{-2}	0.8975	78
	2	1.3090×10^{-1}	0	1.3090×10^{-1}	0.9499	241
	4	6.2505×10^{-1}	0	6.2505×10^{-1}	1.2198	783
	D^{tan}	1.0860×10^{-2}	1.3878×10^{-14}	1.0860×10^{-2}	0.8727	34

4. Numerical examples

Numerical examples are presented in this section to validate the effectiveness of the new DDTO framework. Without loss of generality, the geometric sizes and loads are all dimensionless. The method of moving asymptotes (MMA) [45] is used as the optimizer.

Both traditional topology optimization (TTO) and DDTO frameworks are applied for the sake of comparison. The relative discrepancy of the optimized structures obtained with different frameworks is measured by

$$\delta_A = \frac{1}{m} \sum_{e=1}^m \left| \frac{A_e^{DDTO} - A_e^{TTO}}{A_e^{TTO}} \right| \times 100\% \quad (37)$$

where A_e^{DDTO} and A_e^{TTO} denote the optimized cross-sectional area of bar elements obtained by DDTO and TTO, respectively.

4.1. Two-point loaded plane truss

The 2-point loaded plane truss shown in Fig. 8 is a benchmark problem in truss topology optimization [46]. The ground structure is composed of 10 bar elements with its elemental connectivity listed in Table 3. Concentrated force $F=1$ is applied on the 3rd and 5th nodes. The noisy data sets in Fig. 9 are considered. They are generated by means of the rate straining control method from the Henky and Ogden models [44], respectively. Relevant parameters in Ogden model are $I=2$, $\gamma_1=-\gamma_2=E/(\beta_1-\beta_2)$ with $E=1$, $\beta_1=10.38$, $\beta_2=0.5$. Gauss random noises with a proportion of 2% relative to the base stresses are added. The initial volume of ground structure is 10 and the initial cross-sectional area of each bar element is defined as the ratio between initial volume and the sum of bars' lengths. The objective is to minimize structural end-compliance while material volume limited by $V_{\max}=10$.

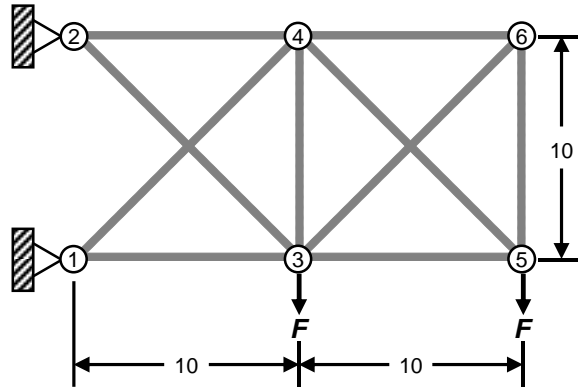


Fig. 8. Schematic of 2-point loaded plane truss.

Table 3. Element connectivity of the 2-point loaded plane truss.

Element no.	1	2	3	4	5	6	7	8	9	10
Node I	1	3	2	1	2	3	5	4	3	4
Node II	3	4	3	4	4	5	6	5	6	6

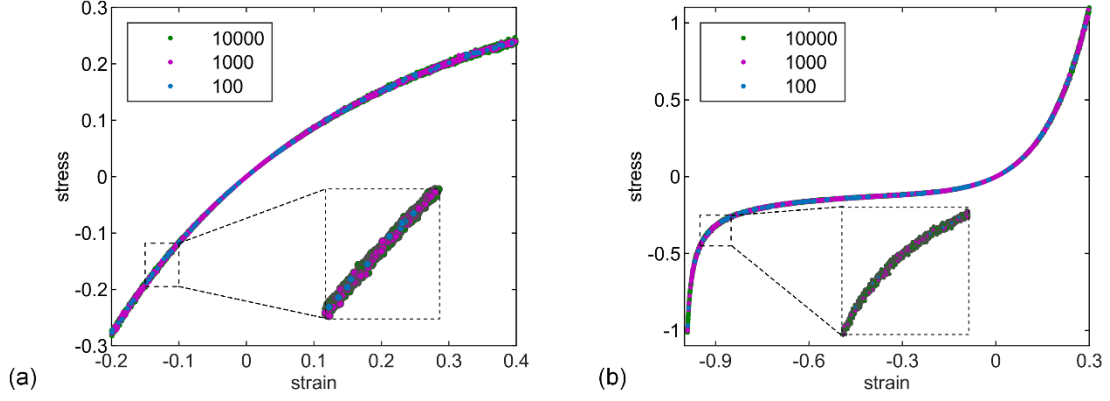


Fig. 9. Material data sets with noises: (a) material I ; (b) material II.

Firstly, suppose the structure is made of material I. Fig. 10(a) shows the tangent modulus D^{tan} calculated by MLS in Eq. (33) when $n=10^4$. The radius of support domain is $d_f=0.05$. The result matches well with that obtained with analytic method. Fig. 10(b) indicates that the maximum error of tangent modulus decreases along with the increase of material data. The optimized results of both DDTO with $n=10^2, 10^3, 10^4, 10^5, 10^6$ and TTO are illustrated in Fig. 11. Corresponding convergence curves of structural end-compliance and volume are shown in Fig. 12. The optimized cross-sectional areas are listed in Table 4. As illustrated in Fig. 13(a), the relative discrepancy of optimized results $\delta(A)$ decreases along with the enlargement of material data set, while the mean CPU time increases dramatically. This is because the cluster analysis method to deal with noisy data is computationally expensive, especially for big data sets. Fig. 13(b) depicts the variation of $\delta(A) \times t_{\text{CPU}}$ in regard to material number. It is illustrated that when $n \geq 10^6$ the computational cost will be significantly increased with limited improvement of the accuracy.

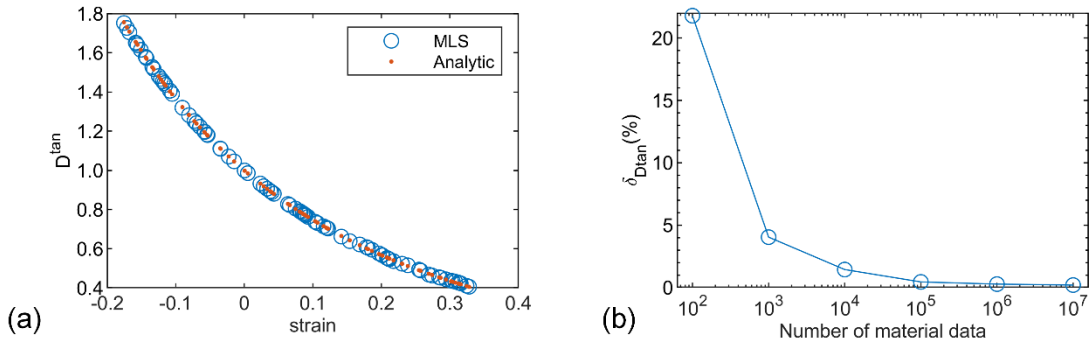


Fig. 10. Material I: (a) tangent modulus D^{tan} calculated by MLS and analytic approaches; (b) relative discrepancy $\delta_{D^{\text{tan}}}$ with respect to the variation of material data number.

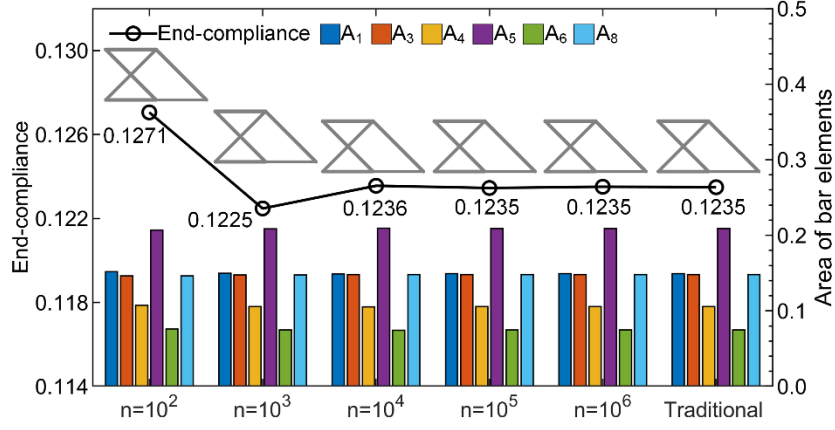


Fig. 11. Optimized results of the DDTO with $n=10^2$, 10^3 , 10^4 , 10^5 , 10^6 and TTO frameworks – material I.

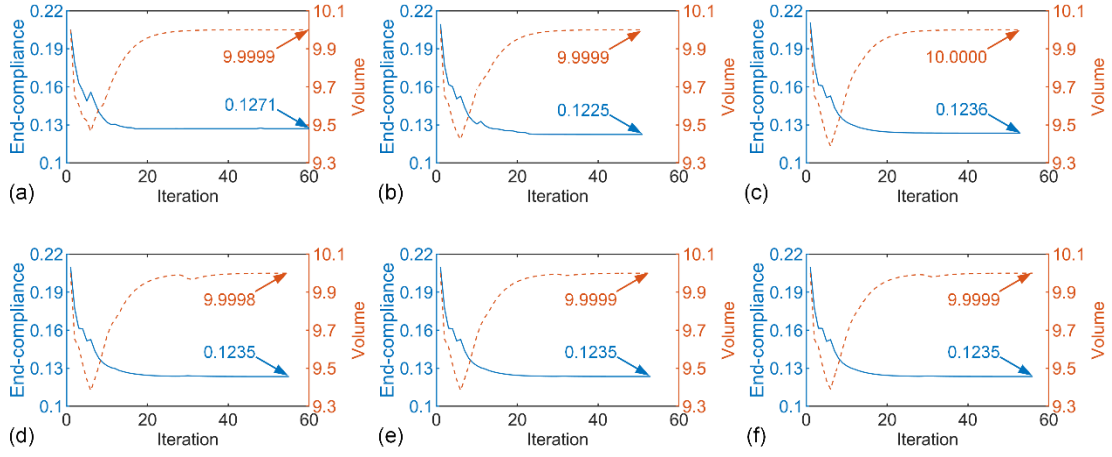


Fig. 12. Convergence curves of structural end-compliance and volume in the case of material I: (a) DDTO ($n=10^2$); (b) DDTO ($n=10^3$); (c) DDTO ($n=10^4$); (d) DDTO ($n=10^5$); (e) DDTO ($n=10^6$); (f) TTO.

Table 4. Optimized results for the plane truss – material I.

	A_1	A_3	A_4	A_5	A_6	A_8	δ_A (%)	$t_{CPU}(s)$
$n=10^2$	0.1517	0.1463	0.1073	0.2069	0.0758	0.1463	1.3732	0.0265
$n=10^3$	0.1495	0.1476	0.1057	0.2087	0.0748	0.1476	0.2230	0.0710
$n=10^4$	0.1489	0.1480	0.1053	0.2093	0.0744	0.1480	0.1355	0.2401
$n=10^5$	0.1492	0.1478	0.1055	0.2090	0.0746	0.1478	0.0404	0.8387
$n=10^6$	0.1491	0.1478	0.1054	0.2091	0.0746	0.1478	0.0035	5.7912
$n=10^7$	0.1491	0.1478	0.1054	0.2091	0.0745	0.1478	0.0099	87.7134
Traditional TO	0.1491	0.1478	0.1054	0.2091	0.0746	0.1478	-	0.0095

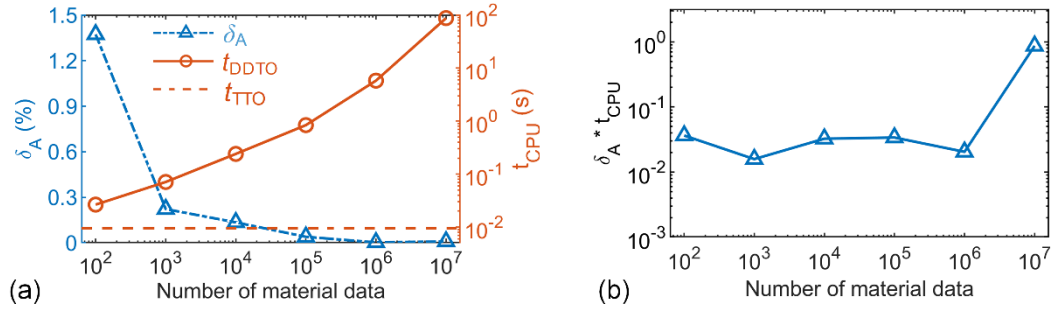


Fig. 13. The variations of δ_A , t_{CPU} and $\delta_A \times t_{CPU}$ along with the increase of material data number - material I: (a) δ_A and t_{CPU} ; (b) $\delta_A \times t_{CPU}$.

Secondly, suppose the structure is made of material II. Similarly, as illustrated in Fig. 14, the maximum error of tangent modulus evaluated by MLS decreases along with the increase of material data. The radius of support domain is $d_I=0.05$. The optimized results of both DDTO with $n=10^3, 10^4, 10^5, 10^6, 10^7$ and TTO are illustrated in Fig. 15. Corresponding convergence curves are shown in Fig. 16. The optimized cross-sectional areas are listed in Table 5. Fig. 17 illustrated $\delta(A)$ and t_{CPU} with respect to material data number. In this case, when $n \geq 10^4$ the computational cost will be significantly increased with limited improvement of the accuracy.

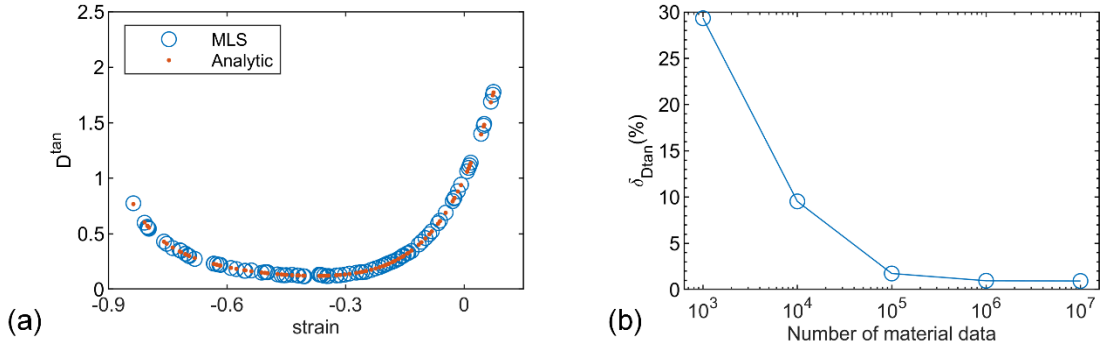


Fig. 14. Material II: (a) tangent modulus D^{\tan} calculated by MLS and analytic approaches; (b) relative discrepancy $\delta_{D^{\tan}}$ with respect to the variation of material data number.

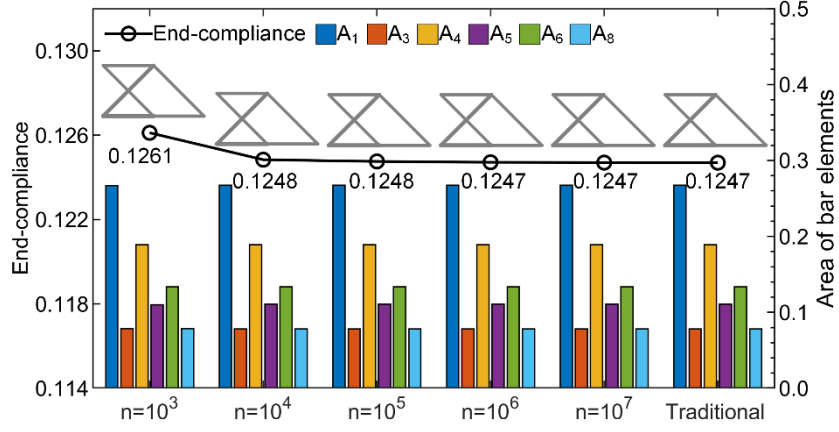


Fig. 15. Optimized results of the DDTO with $n=10^3$, 10^4 , 10^5 , 10^6 , 10^7 and TTO frameworks – material II.

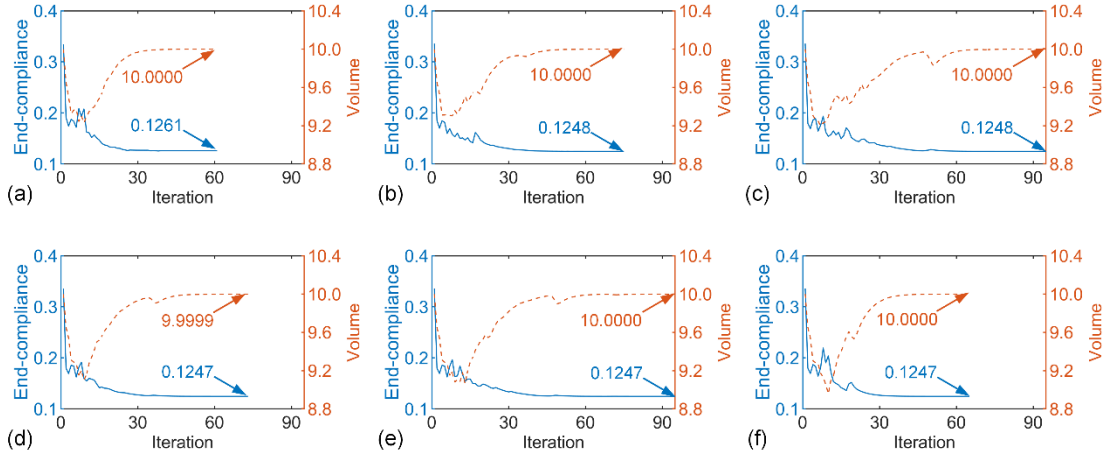


Fig. 16. Convergence curves of structural end-compliance and volume in the case of material II: (a) DDTO ($n=10^3$); (b) DDTO ($n=10^4$); (c) DDTO ($n=10^5$); (d) DDTO ($n=10^6$); (e) DDTO ($n=10^7$); (f) TTO.

Table 5. Optimized results for the plane truss – material II.

	A_1	A_3	A_4	A_5	A_6	A_8	δ_A (%)	$t_{CPU}(s)$
$n=10^3$	0.2671	0.0787	0.1888	0.1097	0.1335	0.0787	0.3836	0.0685
$n=10^4$	0.2673	0.0782	0.1890	0.1106	0.1336	0.0782	0.0079	0.2451
DDTO $n=10^5$	0.2674	0.0781	0.1891	0.1105	0.1337	0.0781	0.0449	0.9364
$n=10^6$	0.2673	0.0782	0.1890	0.1106	0.1336	0.0782	0.0185	10.6770
$n=10^7$	0.2673	0.0782	0.1890	0.1106	0.1336	0.0782	0.0263	103.1261
Traditional TO	0.2673	0.0782	0.1890	0.1106	0.1336	0.0782	-	0.0125

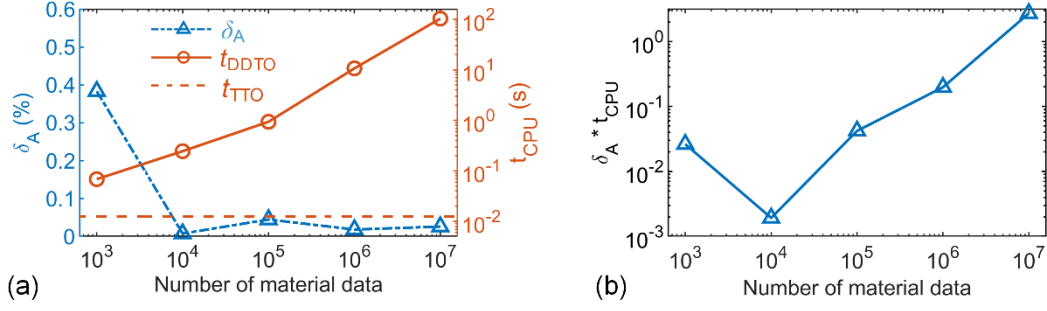


Fig. 17. The variations of δ_A , t_{CPU} and $\delta_A \times t_{CPU}$ along with the increase of material data number - material II: (a) δ_A and t_{CPU} ; (b) $\delta_A \times t_{CPU}$.

4.2. Cantilevered space truss

To further assess the proposed DDTO method, we consider a space truss structure in a box design domain with dimension $L_x \times L_y \times L_z = 3 \times 1 \times 1$, as shown in Fig. 18(a). The structure is fixed at two vertical edges of one end and loaded with $F=1$ at the centroid of the opposite end. In this example, the full-level ground structure in Fig. 18(b) consists of 1618 non-collimated bar elements. Initial cross-sectional area of each bar element is 0.05. The upper limit of volume bound is $V_{\max}=30$.

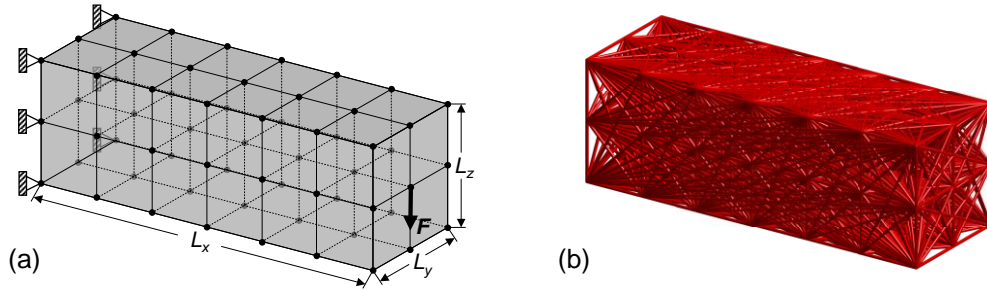


Fig. 18. Schematic of cantilevered space truss: (a) geometry, loading and boundary conditions; (b) full-level ground structure.

4.2.1. Material data sets without noises

As shown in Fig. 19, the material data sets without noises are firstly considered. They correspond to the Ogden model [44] where $I=2$ and $\gamma_1 = -\gamma_2 = E/(\beta_1 - \beta_2)$. Relevant parameters are $E=1$, $\beta_1=187.6$, $\beta_2=-67.9$ for material I and $E=1$, $\beta_1=71.34$, $\beta_2=-181.89$ for material II, respectively.

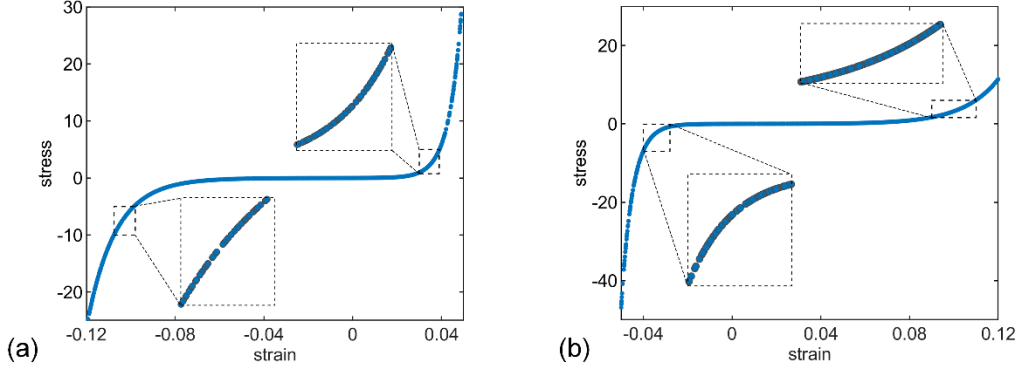


Fig. 19. Material data sets without noises: (a) material I; (b) material II.

To begin with, consider the structure is made of material I. Different material data number is considered where $n=10^3, 10^4, 10^5, 10^6$ and 10^7 . Fig. 20 shows the maximum computing errors of tangent modulus evaluated by MLS decreases with the increase of material data number. In this test, the radius of support domain is $d_I=0.0005$. The convergence curves as well as the optimized results are depicted in Fig. 21. It is observed that the topology optimization process oscillates when $n=10^3$, caused by the computational errors due to the insufficiency of material data. In contrast, the optimization processes converge when $n=10^4, 10^5, 10^6$ and 10^7 . The optimized topologies and cross-sectional areas of DDTO with $n=10^4$ and TTO are compared in Fig. 30, which illustrates the effectiveness of the DDTO method. Fig. 23 illustrates the variations of δ_A and $\delta_A \times t_{CPU}$ in regard to the increase of material data number. The computational cost will be significantly increased with limited improvement of the accuracy when $n \geq 10^6$.

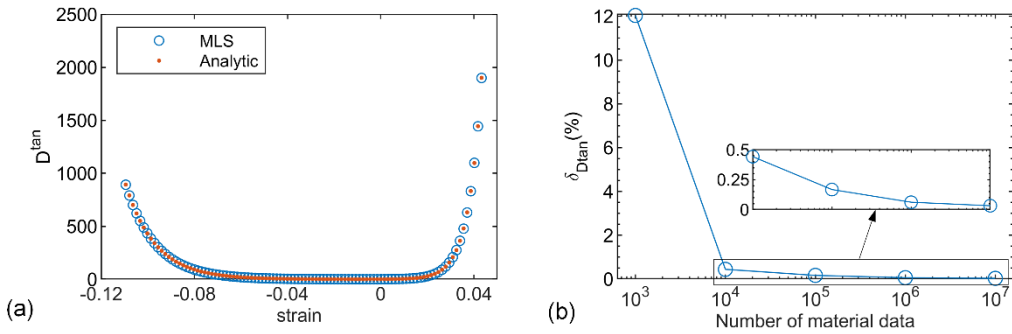


Fig. 20. Material I: (a) tangent modulus D^{\tan} calculated by MLS and analytic approaches; (b) relative discrepancy $\delta_{D^{\tan}}$ with respect to the variation of material data number.

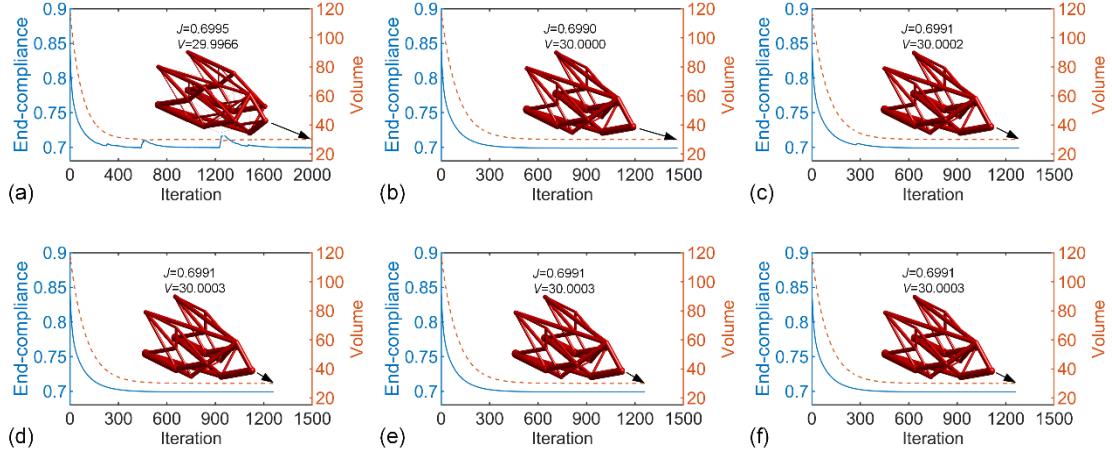


Fig. 21. Convergence curves and optimized results in the case of material I: (a) DDTO ($n=10^3$); (b) DDTO ($n=10^4$); (c) DDTO ($n=10^5$); (d) DDTO ($n=10^6$); (e) DDTO ($n=10^7$); (f) TTO.

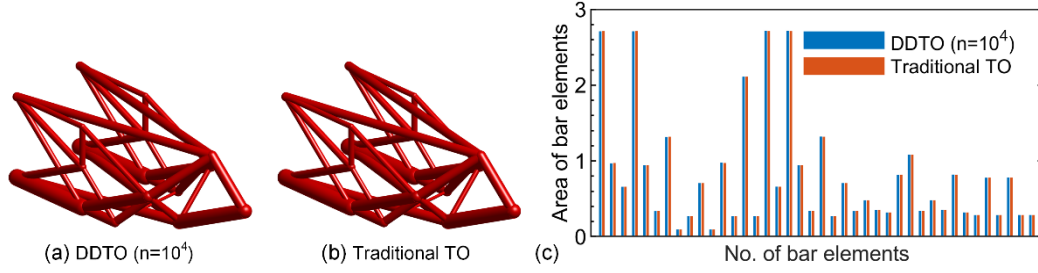


Fig. 22. Comparison of optimized results for the cantilevered space truss in the case of material I: (a) optimized result of DDTO ($n=10^4$); (b) optimized result of TTO; (c) optimized cross-sectional areas of bar elements.

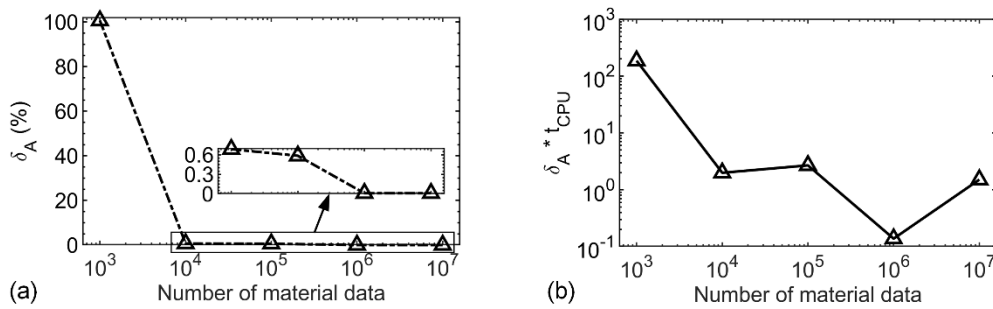


Fig. 23. The variations of δ_A and $\delta_A \times t_{CPU}$ along with the increase of material data number - material I: (a) δ_A ; (b) $\delta_A \times t_{CPU}$.

Besides, material II is tested. The tangent modulus calculation is given in Fig. 24. Convergence curves as well as the optimized results are shown in Fig. 25. The

optimized results of both DDTO with $n=10^4$ and traditional TO are illustrated in Fig. 26. Fig. 27 illustrates the variation of $\delta(A)$ and $\delta(A) \times t_{\text{CPU}}$ with respect to material data number. As in previous case, the computational cost will be significantly increased with limited improvement of the accuracy when $n \geq 10^6$.

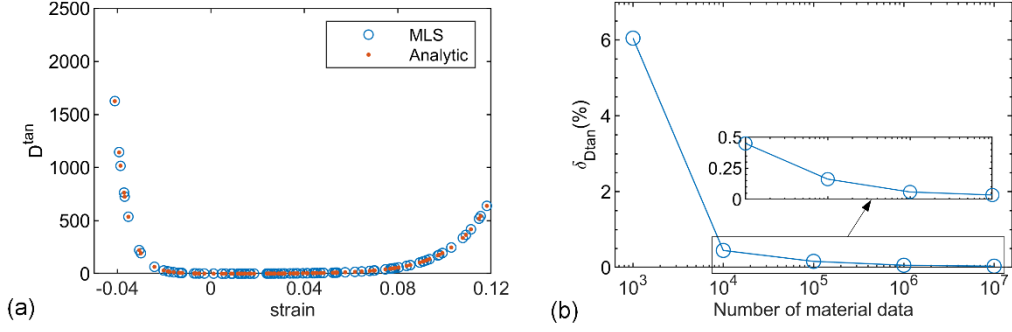


Fig. 24. Material II: (a) tangent modulus D^{tan} calculated by MLS and analytic approaches; (b) relative discrepancy $\delta_{D^{\text{tan}}}$ with respect to the variation of material data number.

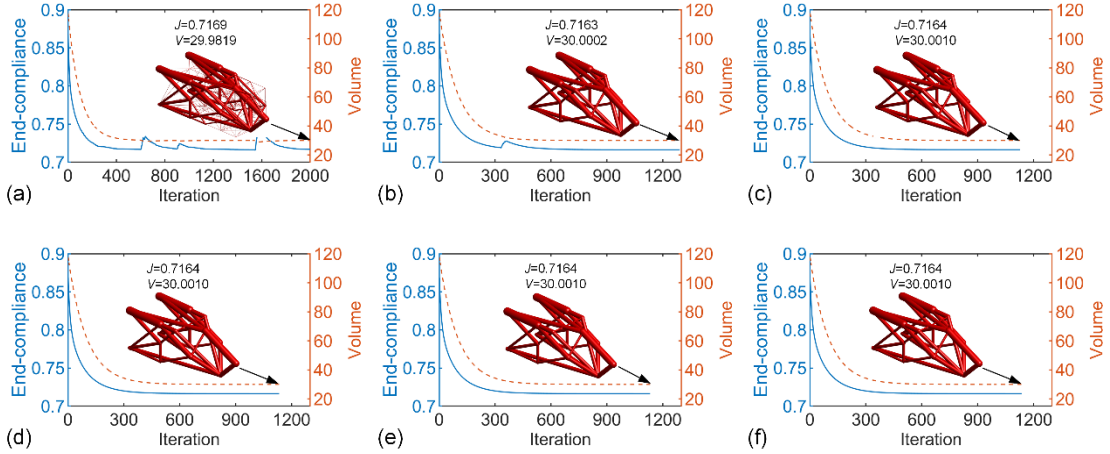


Fig. 25. Convergence curves of structural end-compliance and volume in the case of material II: (a) DDTO ($n=10^3$); (b) DDTO ($n=10^4$); (c) DDTO ($n=10^5$); (d) DDTO ($n=10^6$); (e) DDTO ($n=10^7$); (f) TTO.

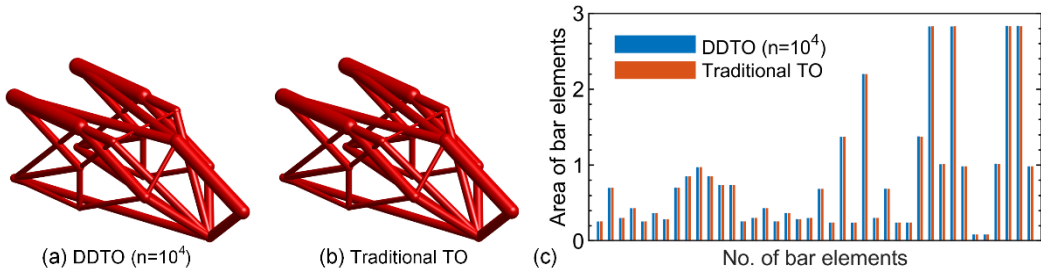


Fig. 26. Comparison of optimized results for the cantilevered space truss in the case of material II: (a) optimized result of DDTO ($n=10^4$); (b) optimized result of TTO; (c) optimized cross-sectional areas of bar elements.

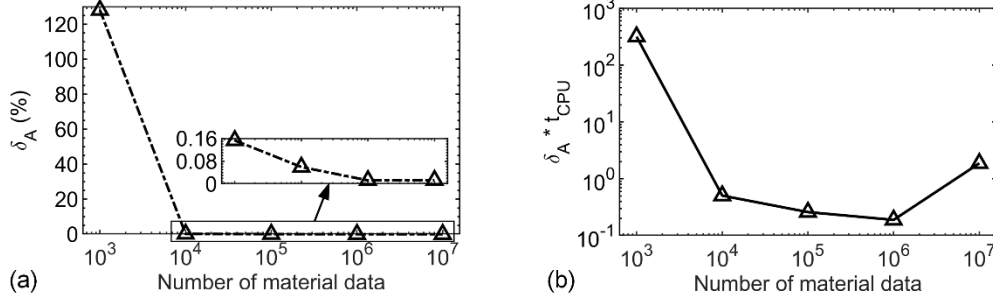


Fig. 27. The variations of δ_A and $\delta_A \times t_{CPU}$ along with the increase of material data number - material II: (a) δ_A ; (b) $\delta_A \times t_{CPU}$.

4.2.2. Material data sets with noises

In the end, noisy data sets are considered. As shown in Fig. 28(a), Gauss random noises with a proportion of 2% relative to the base stresses are added on material I in Fig. 19. Suppose the number of material data $n=10^4$. The tangent modulus in Fig. 28(b) are evaluated by both MLS and analytic methods. The radius of support domain is $d_f=0.005$. The convergence curves along with several intermediate topologies are shown in Fig. 29. Comparisons of the optimized results for both DDTO and traditional TO are given in Fig. 30. The proposed DDTO framework is illustrated to be robust with respect to noisy data sets.

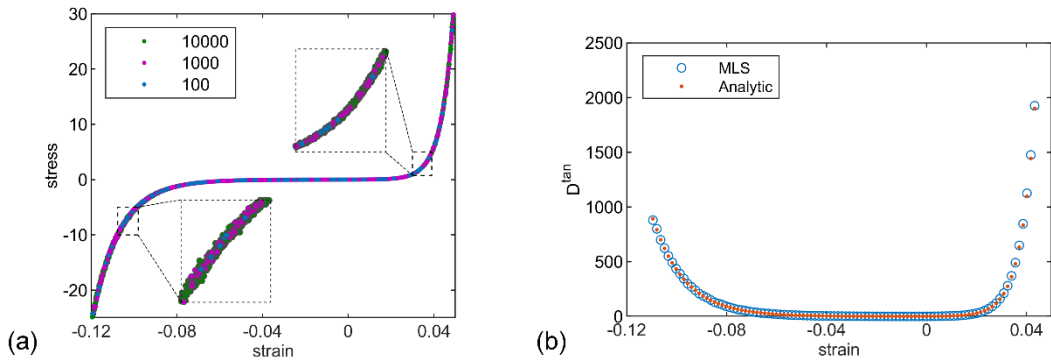


Fig. 28. (a) Material data set with noises – material I; (b) tangent modulus D^{\tan} calculated by MLS and analytic approaches.

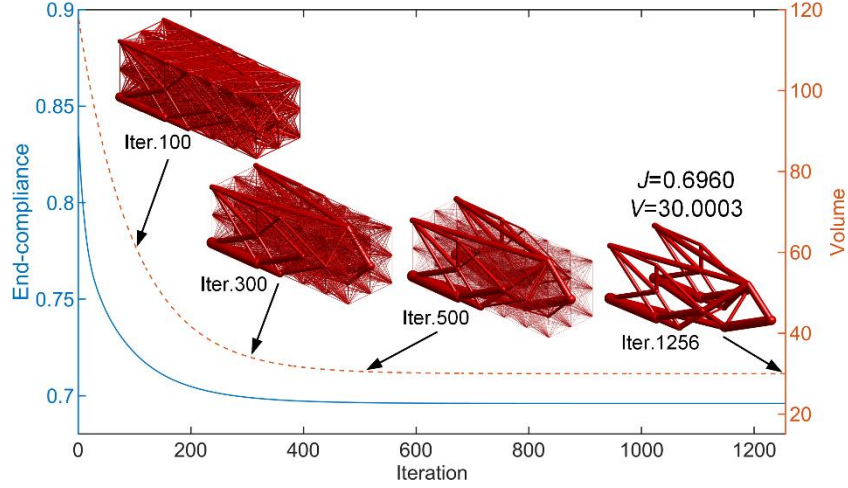


Fig. 29. Convergence curves and intermediate results within the DDTO framework in the case of noisy data set I ($n=10^4$).

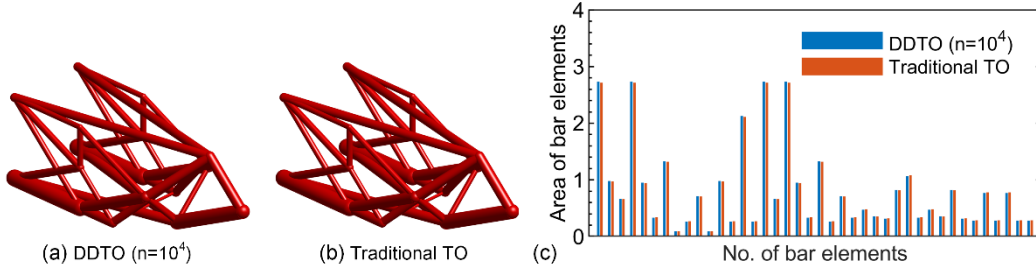


Fig. 30. Comparison of optimized results for the cantilevered space truss in the case of noisy data set I: (a) optimized result of DDTO ($n=10^4$); (b) optimized result of TTO; (c) optimized cross-sectional areas of bar elements.

Similarly, Gauss random noises with a proportion of 2% relative to the base stresses are added on material II in Fig. 19. The noisy data set is depicted in Fig. 31(a). Suppose the number of material data $n=10^4$. The tangent modulus in Fig. 31(b) are evaluated by both MLS and analytic methods. The convergence curves along with several intermediate topologies are shown in Fig. 32. Comparisons of the optimized results for both DDTO and traditional TO are given in Fig. 33.

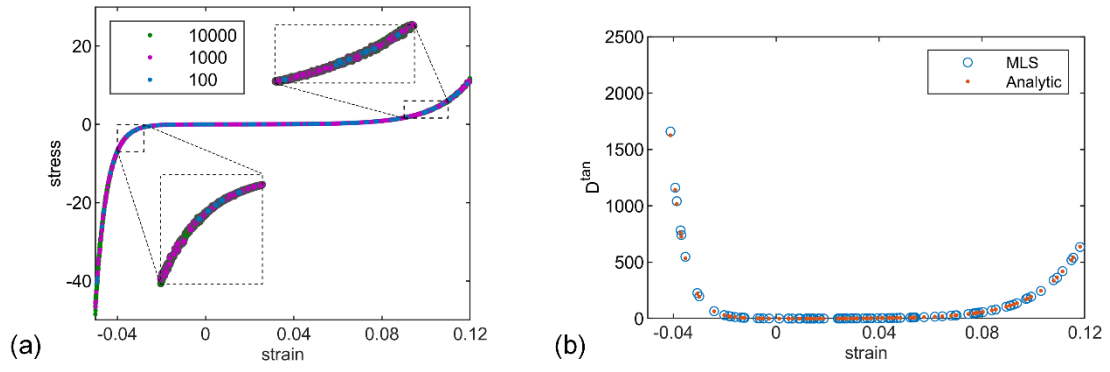


Fig. 31. (a) Material data set with noises – material II; (b) tangent modulus D^{\tan} calculated by MLS and analytic approaches.

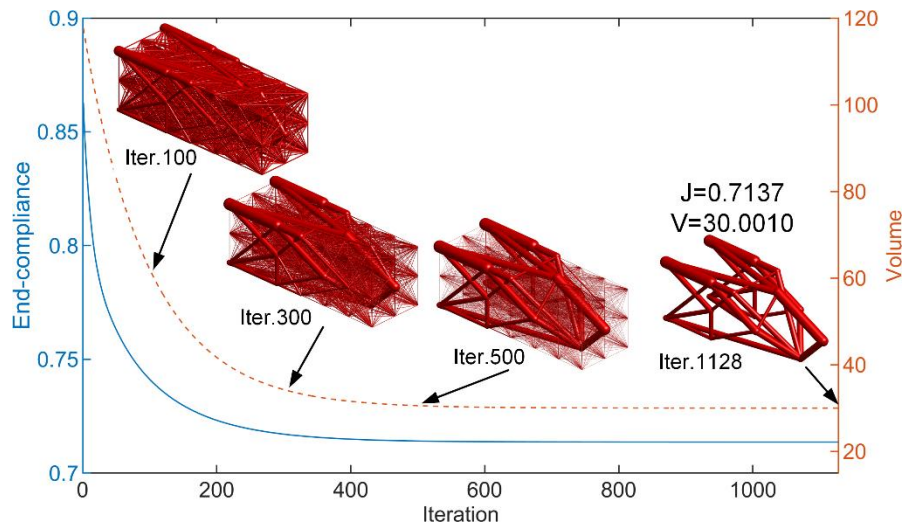


Fig. 32. Convergence curves and intermediate results within the DDTO framework in the case of noisy data set II ($n=10^4$).

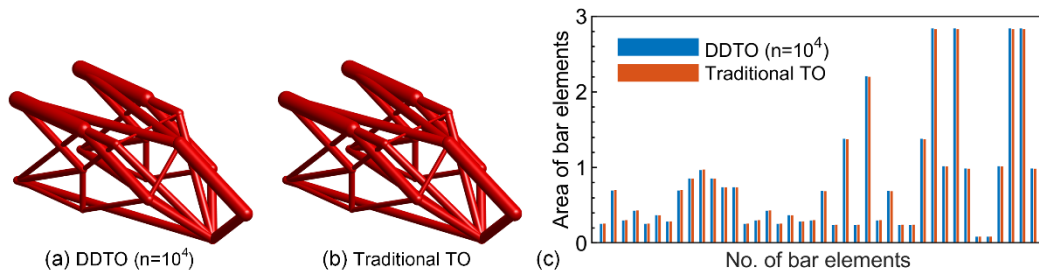


Fig. 33. Comparison of optimized results for the cantilevered space truss in the case of noisy data set II: (a) optimized result of DDTO ($n=10^4$); (b) optimized result of TTO; (c) optimized cross-sectional areas of bar elements.

5. Conclusions

This paper develops a new data-driven topology optimization (DDTO) framework which uses directly discrete material data sets for the description of material behaviors and thus bypasses the usage of constitutive models. The recently developed data-driven computational mechanics is applied for structural analysis, which is robust with respect to noisy data sets by means of cluster analysis techniques. The concept of clustering points is further used to evaluate the tangent modulus with local fitting by means of MLS method. The validity of this new DDTO framework is demonstrated by numerical examples of truss topology optimization. The optimization accuracy and efficiency in regard to the number of material data are investigated. It is shown that positive correlation is observed for optimization accuracy, while negative correlation is seen for efficiency. The optimal number of material data that compromises accuracy and efficiency is problem-dependent and needs numerical investigation for specific problems.

The proposed DDTO framework opens up a new avenue for structural design in current data-rich era, which is appealing in engineering applications with high material nonlinearity. Extension of current framework to continuum structure design is straightforward and will be presented in our following works. It is noteworthy that there are several challenges to be overcome before the DDTO framework becomes a powerful tool for real applications, for instance, effective data analysis algorithms for efficient calculation.

Author Contributions

Y. Z. carried out the calculation, Y. Z., H. Z., W. Z., J. Z., J. B., Q. W. and Y. G. conducted the analysis and discussion.

Conflicts of interest

There are no conflicts of interest to declare.

Acknowledgement

Supports from the Australian Research Council Discovery Projects (DP170102861 and DP180103009) is gratefully acknowledged. This work was supported by the

Queensland University of Technology (QUT) through the use of their high-performance computing facilities.

References

- [1] Sigmund O, Maute K. Topology optimization approaches. *Struct Multidiscip Optim* 2013;48:1031–55.
- [2] Deaton JD, Grandhi RV. A survey of structural and multidisciplinary continuum topology optimization: post 2000. *Struct Multidiscip Optim* 2014;49:1–38.
- [3] Zhu JH, Zhang WH, Xia L. Topology optimization in aircraft and aerospace structures design. *Arch Comput Methods Eng* 2016;23:595–622.
- [4] Huang X, Xie YM. A further review of ESO type methods for topology optimization. *Struct Multidiscip Optim* 2010;41:671–83.
- [5] Zhao ZL, Zhou S, Cai K, Min Xie Y. A direct approach to controlling the topology in structural optimization. *Comput Struct* 2020;227:106141.
- [6] Sotiropoulos S, Kazakis G, Lagaros ND. Conceptual design of structural systems based on topology optimization and prefabricated components. *Comput Struct* 2020;226:106136.
- [7] Kwak J, Cho S. Topological shape optimization of geometrically nonlinear structures using level set method. *Comput Struct* 2005;83:2257–68.
- [8] Buhl T, Pederson CBW, Sigmund O. Stiffness design of geometrically nonlinear structures using topology optimization. *Struct Optim* 2000;19:93–104.
- [9] Gea HC, Luo J. Topology optimization of structures with geometrical nonlinearities. *Comput Struct* 2001;79:1977–85.
- [10] Yoon GH, Kim YY. Element connectivity parameterization for topology optimization of geometrically nonlinear structures. *Int J Solids Struct* 2005;42:1983–2009.
- [11] Wang F, Lazarov BS, Sigmund O, Jensen JS. Interpolation scheme for fictitious domain techniques and topology optimization of finite strain elastic problems. *Comput Methods Appl Mech Eng* 2014;276:453–72.
- [12] Runesson K, Steinmann P, Ekh M, Menzel A. Constitutive modeling of engineering materials—theory and computation. Vol I Gen Concepts Inelasticity 2006.
- [13] Lin YC, Chen XM. A critical review of experimental results and constitutive descriptions for metals and alloys in hot working. *Mater Des* 2011;32:1733–59.

- [14] Bruns TE, Tortorelli DA. Topology optimization of non-linear elastic structures and compliant mechanisms. *Comput Methods Appl Mech Eng* 2001;190:3443–59.
- [15] Klarbring A, Strömberg N. Topology optimization of hyperelastic bodies including non-zero prescribed displacements. *Struct Multidiscip Optim* 2013;47:37–48.
- [16] Ramos AS, Paulino GH. Convex topology optimization for hyperelastic trusses based on the ground-structure approach. *Struct Multidiscip Optim* 2015;51:287–304.
- [17] Chen F, Wang Y, Wang MY, Zhang YF. Topology optimization of hyperelastic structures using a level set method. *J Comput Phys* 2017;351:437–54.
- [18] Lu D, Du X, Wang G, Zhou A, Li A. A three-dimensional elastoplastic constitutive model for concrete. *Comput Struct* 2016;163:41–55.
- [19] Maute K, Ramm E. Adaptive topology optimization of elastoplastic structures. *6th Symp Multidiscip Anal Optim* 1996:1133–41.
- [20] Schwarz S, Maute K, Ramm E. Topology and shape optimization for elastoplastic structural response. *Comput Methods Appl Mech Eng* 2001;190:2135–55.
- [21] Yoon GH, Kim YY. Topology optimization of material-nonlinear continuum structures by the element connectivity parameterization. *Int J Numer Methods Eng* 2007;69:2196–218.
- [22] Bogomolny M, Amir O. Conceptual design of reinforced concrete structures using topology optimization with elastoplastic material modeling. *Int J Numer Methods Eng* 2012;90:1578–97.
- [23] Anitescu C, Atroshchenko E, Alajlan N, Rabczuk T. Artificial neural network methods for the solution of second order boundary value problems. *Comput Mater Contin* 2019;59:345–59.
- [24] Samaniego E, Anitescu C, Goswami S, Nguyen-Thanh VM, Guo H, Hamdia K, et al. An energy approach to the solution of partial differential equations in computational mechanics via machine learning: Concepts, implementation and applications. *Comput Methods Appl Mech Eng* 2020;362:112790.
- [25] Jose R, Ramakrishna S. Materials 4.0: Materials big data enabled materials discovery. *Appl Mater Today* 2018;10:127–32.
- [26] Liu GR. FEA-AI and AI-AI: Two-way deepnets for real-time computations for

- both forward and inverse mechanics problems. *Int J Comput Methods* 2019;16:1–21.
- [27] Liu Z, Bessa MA, Liu WK. Self-consistent clustering analysis: An efficient multi-scale scheme for inelastic heterogeneous materials. *Comput Methods Appl Mech Eng* 2016;306:319–41.
 - [28] Bessa MA, Bostanabad R, Liu Z, Hu A, Apley DW, Brinson C, et al. A framework for data-driven analysis of materials under uncertainty: Countering the curse of dimensionality. *Comput Methods Appl Mech Eng* 2017;320:633–67.
 - [29] Deng B, Tan KBC, Lu Y, Zaw K, Zhang J, Liu GR, et al. Inverse identification of elastic modulus of dental implant-bone interfacial tissue using neural network and FEA model. *Inverse Probl Sci Eng* 2009;17:1073–83.
 - [30] Li H, Kafka OL, Gao J, Yu C, Nie Y, Zhang L, et al. Clustering discretization methods for generation of material performance databases in machine learning and design optimization. *Comput Mech* 2019;64:281–305.
 - [31] White DA, Arrighi WJ, Kudo J, Watts SE. Multiscale topology optimization using neural network surrogate models. *Comput Methods Appl Mech Eng* 2019;346:1118–35.
 - [32] Xia L, Breitkopf P. Multiscale structural topology optimization with an approximate constitutive model for local material microstructure. *Comput Methods Appl Mech Eng* 2015;286:147–67.
 - [33] Hamdia KM, Ghasemi H, Bazi Y, AlHichri H, Alajlan N, Rabczuk T. A novel deep learning based method for the computational material design of flexoelectric nanostructures with topology optimization. *Finite Elem Anal Des* 2019;165:21–30.
 - [34] Kirchdoerfer T, Ortiz M. Data-driven computational mechanics. *Comput Methods Appl Mech Eng* 2016;304:81–101.
 - [35] Conti S, Müller S, Ortiz M. Data-driven problems in elasticity. *Arch Ration Mech Anal* 2018;229:79–123.
 - [36] Kirchdoerfer T, Ortiz M. Data Driven Computing with noisy material data sets. *Comput Methods Appl Mech Eng* 2017;326:622–41.
 - [37] Nguyen LTK, Keip MA. A data-driven approach to nonlinear elasticity. *Comput Struct* 2018;194:97–115.
 - [38] Ibanez R, Abisset-Chavanne E, Aguado JV, Gonzalez D, Cueto E, Chinesta F.

- A manifold learning approach to data-driven computational elasticity and inelasticity. *Arch Comput Methods Eng* 2018;25:47–57.
- [39] Bendsøe MP. *Topology optimization*. Springer; 2009.
- [40] Christensen PW, Klarbring A. *An introduction to structural optimization*. vol. 153. Springer Science & Business Media; 2008.
- [41] Liu GR, Gu YT. *An introduction to meshfree methods and their programming*. Springer Science & Business Media; 2005.
- [42] Lancaster P, Salkauskas K. Surfaces generated by moving least squares methods. *Math Comput* 1981;37:141–58.
- [43] ASTM International. *E8/E8M-13 Standard Test Methods for Tension Testing of Metallic Materials*. West Conshohocken, PA; ASTM Int 2013.
- [44] Ogden RW. *Non-linear elastic deformations*. Courier Corporation; 1997.
- [45] Svanberg K. The method of moving asymptotes—a new method for structural optimization. *Int J Numer Methods Eng* 1987;24:359–73.
- [46] Stolpe M. Truss optimization with discrete design variables: a critical review. *Struct Multidiscip Optim* 2016;53:349–74.